Graz University of Technology
Institute of Theoretical and Computational Physics

ITPR-2011-021CorRev

Reaction Fields of Homogeneous Magnetic Spheroids of Arbitrary Direction in a Homogeneous Magnetic Field. A Toolbox for MRI and MRS of Heterogeneous Tissue

Markus Kraiger * Bernhard Schnizer †

December 2011, revised October 2012, corrected 2014-01-14

Technische Universität Graz
Institut für Theoretische Physik - Computational Physics
Institute of Medical Engineering

*Institute of Medical Engineering, Technische Universität Graz, Kronesgasse 5 , A-8010 Graz
†Inst. f. Theoretische Physik-Computational Physics, Technische Universität Graz, Petersgasse 16, A-8010 Graz

ITPR – Berichte
Eigentümer, Herausgeber, Verleger:
Institut für Theoretische Physik
der Technischen Universität Graz
Für den Inhalt verantwortlich:
Em.Univ. Prof. Dr. B. Schnizer
und Dr. M. Kraiger
Petersgasse 16, A-8010 Graz.

Abstract

The reaction fields of homogeneous magnetic prolate and oblate spheroids of arbitrary direction of the symmetry axis in a given external homogeneous magnetic field are expressed in Cartesian coordinates. At first the total potentials and fields are computed in common prolate or oblate spheroidal coordinates for an arbitrary direction of the external magnetic field following Kuchel and Bullimann (1989). The potentials so obtained are transformed to Cartesian coordinates in such a way that their dependencies on the invariants of rotations around the symmetry axis become obvious. These results are generalized to arbitrary directions of both the symmetry axis and of the field axis. The fields are computed by taking gradients and expressing these again by the invariants. – The advantage of this new approach is that it is very easy to build and investigate structures built from spheroids with different axes and positions. There is no need of complicated coordinate transformations. Two applications from the area of MR-Osteodensitometry are shown: i) modelling of bone loss within plate-like trabecular structures ; ii) microcracks in bone structures as examples of trabecular rarefication.

Contents

1 Introduction

Magnetic resonance imaging (MRI) and magnetic resonance spectroscopy (MRS) make use of the Larmor resonance signals emitted by protons precessing in the local magnetic induction, which is provided by an external static magnetic field. In general, the MR signal is highly sensitive to the magnetic properties of the matter surrounding the nuclei. Theoretical studies of the resonance signal behaviour in situations of varying magnetic susceptibilities and dynamic physiological processes as for instance diffusion utilize the analytical magnetostatic solutions of specific geometrical bodies. Models of structures like cells or blood vessels can be built up from arrays of such simple magnetic bodies. In particular prolate and oblate spheroids are used as such building blocks to analyse the local magnetic field distribution in the vicinity of blood cells in MRS of cells [1]. In that previous work the reaction fields are computed for spheroids with the z-axis as the symmetry axis and a homogeneous static external field of arbitrary direction. In the current work we derive formulas in Cartesian coordinates for arbitrary directions of both the symmetry axis and of the external magnetic field. This grants still more freedom, flexibility and ease for building complex structures composed of arbitrarily arranged spheroids.

We gain these solutions starting from the expressions for the reaction field potentials in spheroidal coordinates derived in [1]. There the expressions for the potentials and the fields have also been expressed in Cartesian coordinates except for three functions in $\cosh\eta$ (in the prolate case) or in $\sinh\eta$ (in the oblate case), where η is the quasiradial variable. We succeed in replacing these hyperbolic functions by square root expressions involving Cartesian coordinates. These square roots depend on the square of the radius, a rotation invariant, and on z^2, which is invariant under rotations around the symmetry axis. All other terms of the potentials depend on similar invariants. This dependences permit one to go from the $z-$axis to an arbitrary vector as the symmetry axis.

The gradients of the potentials are needed to determine the field expressions. For this purpose the gradients of the three functions occuring in the potentials are computed and simplified. In this way a toolbox for MRI and MRS resonance signal analyses with flexible instruments is provided capable of modelling several biological tissues of interest such as trabecular bone, microvascular network and general interfaces of adjacent tissues.

Inserting a prolate or oblate spheroid into the primary homogeneous field produces a reaction fields within and near the spheroid. This process may be described by tensors transforming the primary magnetic field into the reaction fields. Theses tensors are given in Chap.5. This provides also the opportunity to give a very concise presentation of all the formulas needed to express the reactions.

The version ITPR-2011-02rev differs from the first version (ITPR-2011-02) inasmuch as a severe typographical error has been corrected in eq.(3.6); $\mathrm{Arcoth}(a_p/c_p)$ is replaced

with $\mathrm{Arcoth}(c_p/a_p)$.
In addition, a new chapter has been inserted; which is numbered Chapter 5. It contains the tensors transforming the primary potential into that of the reaction, and other tensors transforming the primary field into the reaction field. The applications are now in Chapter 6.

The latest version of this report and of the corresponding *Mathematica* notebooks are displayed on the website [2].

2 The Primary Field

The primary field is a homogeneous static magnetic field. In the general case this may be written as

$$\mathbf{H}_0 \quad = \quad (H_{0x}, H_{0y}, H_{0z}) \tag{2.1}$$

with the corresponding potential

$$\Phi_0(x, y, z) \;=\; -\,(H_{0x}\; x \;+\; H_{0y}\; y \;+\; H_{0z}\; z). \tag{2.2}$$

3 A Single Prolate Spheroid in a Homogeneous Magnetic Field

A prolate spheroid (semi-axes $a_p, a_p, c_p;\ c_p > a_p$) with magnetic susceptibility $\mu_2 = \mu_0(1+\chi_2)$ is in a medium with magnetic susceptibility $\mu_1 = \mu_0(1+\chi_1)$ and in an external field (2.1). The solution of this boundary value problem has been very well explained in ref. [1]. This is summarized in sect. 3.1 but the expansion coefficients are denoted a little different from the notation used in this ref. In the subsequent sections these results are extended to an arbitrary direction of the symmetry axis.

3.1 The reaction field in prolate spheroidal coordinates

The spheroid induces a reaction field represented by the potentials $\Phi_{r1}(x,y,z)$ in the exterior, by $\Phi_{r2}(x,y,z)$ in the interior. This problem is solved in prolate spheroidal coordinates (s., for example, Fig.1.06 of ref.[3])

$$x = e_p \sinh\eta \ \sin\theta \ \cos\psi, \tag{3.1}$$

$$y = e_p \sinh\eta \ \sin\theta \ \sin\psi, \tag{3.2}$$

$$z = e_p \cosh\eta \ \cos\theta; \tag{3.3}$$

$$e_p = \sqrt{c_p^2 - a_p^2} \tag{3.4}$$

for a spheroid, whose symmetry axis coincides with the z-axis. $\Phi_0,\ \Phi_1 = \Phi_0 + \Phi_{r1},\ \Phi_2 = \Phi_0 + \Phi_{r2}$ must be solutions of the potential equation in prolate coordinates. This partial differential equation can be solved by separation.

$$\Phi(\eta,\theta,\psi) = H(\eta)\ \Theta(\theta)\ \Psi(\psi). \tag{3.5}$$

The particular solutions of the resulting equation for the quasi-radial functions $H(\eta)$ are Legendre polynomials or functions in $\cosh\eta$. The solutions $\Theta(\theta)$ must be Legendre polynomials in $\cos\theta$; Legendre functions in $\cos\theta$ are singular at $\theta = 0, \pi$; so they must be excluded. $\Psi(\psi)$ are trigonometric functions in ψ.

The interface separating the two domains is the spheroid:

$$\frac{x^2}{a_p^2} + \frac{y^2}{a_p^2} + \frac{z^2}{c_p^2} = 1 \quad \Leftrightarrow \quad \eta = \eta_p = \mathrm{Arcoth}(c_p/a_p). \tag{3.6}$$

A typographical error η_p =Arcoth(a_p/c_p) occured in the first edition (December2011) of this report. This error is also in ref.[4] but not in ref.[5].

The potentials must be continuous across this interface:

$$\eta = \eta_p : \quad \Phi_1 = \Phi_2; \tag{3.7}$$

and there the normal derivatives must fulfil the condition:

$$\eta = \eta_p : \quad \mu_1 \, \partial\Phi_1/\partial\eta \;=\; \mu_2 \, \partial\Phi_2/\partial\eta. \tag{3.8}$$

One starts inserting the spheroidal coordinates into the primary potential (2.2). Thereafter these are replaced by the corresponding particular solutions to give:

$$\begin{aligned}\Phi_0 \;=\; & - e_p \; P_1^1(\cosh\eta) \; P_1^1(\cos\theta) \; (H_{0x}\cos\psi + H_{0y}\sin\psi) \\ & - e_p \; P_1^0(\cosh\eta) \; P_1^0(\cos\theta) \; H_{0z}.\end{aligned} \tag{3.9}$$

The general solutions for the total field are expressed as expansions in all the particular solutions compatible with the following boundary conditions: 1) The total field must be finite at the origin; 2) the reaction field must be zero at infinity. This leads to the following series expansions:

$$\begin{aligned}& \eta \geq \eta_p : \\ & \Phi_1 \;=\; - e_p \; H_{0z} \; P_1^0(\cosh\eta) \; P_1^0(\cos\theta) \; - \\ & \qquad - e_p \; (H_{0x} \; \cos\psi + H_{0y} \; \sin\psi) P_1^1(\cosh\eta) \; P_1^1(\cos\theta) \; + \\ & \qquad + \sum_{n=0}^{\infty}\sum_{m=0}^{\infty} \; {}_1A_n^m \; Q_n^m(\cosh\eta) P_n^m(\cos\theta)\cos(m\psi) \; + \\ & \qquad + \sum_{n=1}^{\infty}\sum_{m=1}^{\infty} \; {}_1B_n^m \; Q_n^m(\cosh\eta) P_n^m(\cos\theta)\sin(m\psi);\end{aligned} \tag{3.10}$$

$$\begin{aligned}& \eta \leq \eta_p : \\ & \Phi_2 \;=\; \sum_{n=0}^{\infty}\sum_{m=0}^{\infty} \; {}_2A_n^m \; P_n^m(\cosh\eta) P_n^m(\cos\theta)\cos(m\psi) \; + \\ & \qquad + \sum_{n=1}^{\infty}\sum_{m=1}^{\infty} \; {}_2B_n^m \; P_n^m(\cosh\eta) P_n^m(\cos\theta)\sin(m\psi).\end{aligned} \tag{3.11}$$

The series for the potentials are inserted into the continuity conditions (3.7) and (3.8). In view of the orthogonality of the Legendre polynomials $P_n^m(\cos\theta)$ and of the trigonometric functions these two conditions involving infinite sums are decomposed into an infinite system of finite conditions each one comprising just a single pair of the parameters n and m. For $n \neq 1$ and $m \neq 0$ nor $\neq 1$ these systems are linear homogeneous equations for the unknown coefficients ${}_2A_n^m, {}_2B_n^m, {}_1A_n^m$ and ${}_1B_n^m$ giving zero solutions. Only for $n = 1$ and $m = 0, 1$ one gets inhomogeneous equations with the solutions:

$$
\begin{aligned}
{}_1A_1^0 &= \frac{e_p\ H_{0z}\ (\mu_2 - \mu_1)\ P_1^0\ P_1^{0'}}{\mu_2\ P_1^{0'}\ Q_1^0\ -\ \mu_1\ P_1^0\ Q_1^{0'}} \\
&:= e_p\ H_{0z}\ L_0, && (3.12) \\
{}_2A_1^0 &= e_p\ H_{0z}\ \mu_1\ \left(\frac{P_1^{0'}\ Q_1^0\ -\ P_1^0\ Q_1^{0'}}{\mu_1\ P_1^0\ Q_1^{0'}\ -\ \mu_2\ P_1^{0'}\ Q_1^0}\right) \\
&:= e_p\ H_{0z}\ M_0; && (3.13) \\
{}_1A_1^1 &= \frac{e_pH_{0x}\ (\mu_2 - \mu_1)\ P_1^1\ P_1^{1'}}{\mu_2\ P_1^{1'}\ Q_1^1\ -\ \mu_1\ P_1^1\ Q_1^{1'}} \\
&:= e_p\ H_{0x}\ L_1, && (3.14) \\
{}_1B_1^1 &= e_p\ H_{0y}\ L_1, && (3.15) \\
{}_2A_1^1 &= e_p\ H_{0x}\ \mu_1\ \left(\frac{P_1^{1'}\ Q_1^1\ -\ P_1^1\ Q_1^{1'}}{\mu_1\ P_1^1\ Q_1^{1'}\ -\ \mu_2\ P_1^{1'}\ Q_1^1}\right) \\
&:= e_p\ H_{0x}\ M_1, && (3.16) \\
{}_2B_1^1 &= e_p\ H_{0y}\ M_1. && (3.17)
\end{aligned}
$$

The argument of all the Legendre polynomials and functions in the above equations is $\cosh\eta_p$. The solutions above and further transformations given below have been obtained with the help of *Mathematica*.The corresponding notebook named ProlateCoefficientsRev.nb can be found at the website [2] (cf. eqs.(A21) to (A24) of ref.[1]); it is easy to go over to the more general case where both H_{0x} and $H_{0y} \neq 0$.) In the same reference it has been shown that the Legendre functions and polynomials may be replaced with elementary functions ([1] , eqs.(A25)):

$$
\begin{aligned}
&\eta \geq \eta_p : \\
&\quad \Phi_{r1} = e_p\ (H_{0x}\ \cos\psi + H_{0y}\sin\psi) \times && (3.18) \\
&\qquad \times\ L_1\,(\sinh\eta\ \mathrm{Arcoth}(\cosh\eta) - \coth\eta)\sin\theta \\
&\qquad +\ e_p\ H_{0z}\ L_0\ \ (\cosh\eta\ \mathrm{Arcoth}(\cosh\eta) - 1)\cos\theta\ , \\
&\eta \leq \eta_p : \\
&\quad \Phi_{r2} = e_p\ (M_1+1)(H_{0x}\ \cos\psi + H_{0y}\sin\psi)\ \sinh\eta\ \sin\theta && (3.19) \\
&\qquad +\ e_p\ (M_0+1)\ H_{0z}\ \cosh\eta\ \cos\theta.
\end{aligned}
$$

Making the same substitutions in the definitions of the constants L_0, L_1, M_0, M_1 above and going over to the susceptibilities the expressions for these constants become:

$$L_0 = L_0^p = \frac{(\chi_1 - \chi_2)\cosh\eta_p}{1 + \chi_2 - (1+\chi_1)\coth^2\eta_p + (\chi_1-\chi_2)\cosh(\eta_p)\mathrm{Arcoth}(\cosh\eta_p)}, \tag{3.20}$$

$$L_1 = L_1^p = \frac{\chi_1 - \chi_2}{(2+\chi_1+\chi_2)\ \mathrm{csch}^2\eta_p\ \mathrm{sech}\eta_p + (\chi_1-\chi_2)\big(\mathrm{Arcoth}(\cosh\eta_p) - \mathrm{sech}\eta_p\big)}, \tag{3.21}$$

$$M_0 = M_0^p = -\frac{1 + \chi_1}{1+\chi_1 + (\chi_1-\chi_2)\sinh^2\eta_p\,(1-\cosh\eta_p\ \mathrm{Arcoth}(\cosh\eta_p))}, \tag{3.22}$$

$$M_1 = M_1^p = -\frac{2\ (1 + \chi_1)}{(2+\chi_1+\chi_2) - (\chi_1-\chi_2)\sinh^2\eta_p\,(1-\cosh\eta_p\ \mathrm{Arcoth}(\cosh\eta_p))}. \tag{3.23}$$

The various functions depending on η_p may be replaced by expressions depending only on the semi-axes a_p, c_p. The necessary relations are found from the coordinate transformations (3.1) to (3.4):

$$\begin{array}{lllllll} \sinh(\eta_p) & \to & a_p/e_p, & \quad & \cosh(\eta_p) & \to & c_p/e_p, \\ \mathrm{sech}(\eta_p) & \to & e_p/c_p, & & \mathrm{csch}(\eta_p) & \to & e_p/a_p, \\ \coth(\eta_p) & \to & c_p/a_p. & & & & \end{array} \tag{3.24}$$

So the coefficients L_0, L_1, M_0, M_1 become finally:

$$\begin{aligned}
L_0^p &= [(\chi_1-\chi_2)c_p/e_p]/D_0^p, && (3.25)\\
D_0^p &= 1+\chi_2-(1+\chi_1)c_p^2/a_p^2 + (\chi_1-\chi_2)\,d_p c_p/a_p; \\
L_1^p &= [\chi_1 - \chi_2]/D_1^p, && (3.26)\\
D_1^p &= (2+\chi_1+\chi_2) - (\chi_1-\chi_2)\ a_p^2/e_p^2\ (1-d_p c_p/e_p). \\
M_0^p &= -\ (1 + \chi_1)/D_2^p, && (3.27)\\
D_2^p &= 1+\chi_1 + (\chi_1-\chi_2)\ a_p^2/e_p^2\ (1-d_p c_p/e_p); \\
M_1^p &= [-\ 2\ (1 + \chi_1)]/D_1^p. && (3.28)\\
d_p &= \mathrm{Arcoth}(c_p/e_p). && (3.29)
\end{aligned}$$

Inserting eqs.(3.1) to (3.3) into the reaction potentials Φ_{r1}, (3.18), and Φ_{r2}, (3.19), the latter may be rewritten as:

$$\Phi_{1r}(x,y,z) = \big(H_{0x}\ x + H_{0y}\ y\big)L_1(f_1-f_2) + H_{0z}\ z\ L_0(f_1-f_3), \tag{3.30}$$

$$\Phi_{2r}(x,y,z) = \big(H_{0x}\ x + H_{0y}\ y\big)(M_1+1) + H_{0z}\ z\ (M_0+1). \tag{3.31}$$

The functions f_1, f_2, f_3 depend solely on the function $\cosh\eta$:

$$f_1 = \mathrm{Arcoth}(\cosh\eta), \tag{3.32}$$

$$f_2 = \frac{\cosh\eta}{\sinh^2\eta}, \tag{3.33}$$

$$f_3 = \frac{1}{\cosh\eta}. \tag{3.34}$$

In the exterior of the spheroid is $\eta \geq \eta_p > 1$; so the three functions just introduced are well-defined, real, finite and non-zero in the exterior of the spheroid. This is also shown in Figs.3.1 and 3.2.

If both media are the same both reaction potentials must be zero. Indeed, the limits of the four coefficients

$$\chi_2 \;\to\; \chi_1: \quad L_0 \to 0,\; L_1 \to 0,\; M_0 \to -1,\; M_1 \to -1 \tag{3.35}$$

ensure this.

3.2 The reaction field in Cartesian coordinates

We want expressions for the potential which depend on x, y, z only. So $\cosh\eta$ must be replaced with a corresponding expression in Cartesian coordinates. From eqs.(3.1) to (3.3) one finds:

$$\cosh^2\eta \;=\; \frac{1}{2}\left(1 + \frac{r^2}{e_p^2} \pm \sqrt{\left(1+\frac{r^2}{e_p^2}\right)^2 - 4\frac{z^2}{e_p^2}}\right).$$

Intense numerical studies show that only the plus sign applies. So we have:

$$\cosh\eta \;=\; \frac{1}{\sqrt{2}}\sqrt{1 + \frac{r^2}{e_p^2} + w_p(\mathbf{r},\mathbf{e}_z)} \;:=\; u_p(\mathbf{r},\mathbf{e}_z)/\sqrt{2}, \tag{3.36}$$

$$w_p(\mathbf{r},\mathbf{e}_z) \;=\; \sqrt{\left(1+\frac{r^2}{e_p^2}\right)^2 - 4\frac{z^2}{e_p^2}} \;=\; \sqrt{\left(1+\frac{r^2}{e_p^2}\right)^2 - 4\frac{(\mathbf{e}_z\cdot\mathbf{r})^2}{e_p^2}}, \tag{3.37}$$

$$r^2 \;=\; x^2 + y^2 + z^2 \;=\; \rho^2 + z^2. \tag{3.38}$$

Inserting this expression for $\cosh\eta$ into eqs.(3.32) to (3.34) and inserting the resulting expressions for f_1, f_2, f_3, namely $\tilde{f}_1, \tilde{f}_2, \tilde{f}_3$:

$$\tilde{f}_1 \;=\; \mathrm{Arcoth}(u_p(\mathbf{r},\mathbf{e}_z)/\sqrt{2}), \tag{3.39}$$

$$\tilde{f}_2 \;=\; \frac{\sqrt{2}\; u_p(\mathbf{r},\mathbf{e}_z)}{u_p(\mathbf{r},\mathbf{e}_z)^2 - 2}, \tag{3.40}$$

$$\tilde{f}_3 \;=\; \frac{\sqrt{2}}{u_p(\mathbf{r},\mathbf{e}_z)}. \tag{3.41}$$

into eq.(3.30) we get the final expression for the exterior potential as a pure function of the Cartesian coordinates x, y, z:

$$\Phi_{r1}(x,y,z) \;=\; (H_{0x}\; x \;+ H_{0y}\; y)\; L_1\; (\tilde{f}_1 - \tilde{f}_2) \;+\; H_{0z}\; z\; L_0\; (\tilde{f}_1 - \tilde{f}_3). \tag{3.42}$$

As stated after eqs.(3.34) these functions encounter no problems in the exterior of the spheroid. The interior potential, eq.(3.31), is already a simple function of the Cartesian coordinates.

3.3 Potential and field for an arbitrary direction of the spheroidal symmetry axis

For applications it is necessary to consider spheroids whose symmetry axis has an arbitrary direction. The corresponding expressions for the potential will be derived from those given in eqs.(3.42) and (3.31). These are rewritten in a way suggesting a general form:

$$\begin{aligned} \Phi_{r1}(x,y,z) &= (\mathbf{H}_{0\perp}\cdot\mathbf{r}_\perp)\,L_1\,(\tilde{f}_1-\tilde{f}_2) \;+\; (\mathbf{H}_{0\|}\cdot\mathbf{r}_\|)\,L_0\,(\tilde{f}_1-\tilde{f}_3),\\ \Phi_{r2}(x,y,z) &= (\mathbf{H}_{0\perp}\cdot\mathbf{r}_\perp)\,(M_1+1) \;+\; (\mathbf{H}_{0\|}\cdot\mathbf{r}_\|)(M_0+1). \end{aligned} \tag{3.43}$$

The vectors $\mathbf{H}_{0\|}, \mathbf{r}_\|$ give the projections of the corresponding vectors on the symmetry axis, i.e. the z-axis. Similarly, the vectors $\mathbf{H}_{0\perp} = (H_{0x}, H_{0y}, 0)$, $\mathbf{r}_\perp = (x, y, 0)$ give the vectors corresponding to the projection onto the x,y-plane, which is perpendicular to the symmetry axis.

Now it is easy to accomplish the substitutions for an arbitrary direction of the symmetry axis given by the unit vector $\mathbf{n}$.

$$\begin{aligned} \mathbf{H}_{0\|} &= \mathbf{n}\,(\mathbf{n}\cdot\mathbf{H}_0), \qquad & \mathbf{H}_{0\perp} &= \mathbf{H}_0-\mathbf{H}_{0\|}\;;\\ \mathbf{r}_\| &= \mathbf{n}\,(\mathbf{n}\cdot\mathbf{r}), & \mathbf{r}_\perp &= \mathbf{r}-\mathbf{r}_\|\;. \end{aligned} \tag{3.44}$$

In $w_p(\mathbf{r},\mathbf{e}_z)$ and $w_p(\mathbf{r},\mathbf{e}_z)$, eq.(3.36) and (3.37), only the variable $z = (\mathbf{e}_z\cdot\mathbf{r})$, the component of the position vector along $\mathbf{e}_z$, must be replaced by $(\mathbf{n}\cdot\mathbf{r})$ giving:

$$\cosh\eta \;=\; \frac{1}{\sqrt{2}}\sqrt{1+\frac{r^2}{e_p^2}+\bar{w}_p(\mathbf{r},\mathbf{n})} \;:=\; \bar{u}_p(\mathbf{r},\mathbf{n})/\sqrt{2}, \tag{3.45}$$

$$\bar{w}_p(\mathbf{r},\mathbf{n}) \;=\; \sqrt{\left(1+\frac{r^2}{e_p^2}\right)^2-4\frac{(\mathbf{n}\cdot\mathbf{r})^2}{e_p^2}}. \tag{3.46}$$

The functions $\tilde{f}_i$, eqs.(3.39) to (3.41), remain the same except that $u_p(\mathbf{r},\mathbf{e}_z)$ and $w_p(\mathbf{r},\mathbf{e}_z)$ must be replaced with $\bar{u}_p(\mathbf{r},\mathbf{n})$ and $\bar{w}_p(\mathbf{r},\mathbf{n})$ giving the new functions $\bar{f}_i$:

$$\bar{f}_1 \;=\; \mathrm{Arcoth}(\bar{u}_p(\mathbf{r},\mathbf{n})/\sqrt{2}), \tag{3.47}$$

$$\bar{f}_2 \;=\; \frac{\sqrt{2}\;\bar{u}_p(\mathbf{r},\mathbf{n})}{\big(\bar{u}_p(\mathbf{r},\mathbf{n})\big)^2-2}, \tag{3.48}$$

$$\bar{f}_3 \;=\; \frac{\sqrt{2}}{\bar{u}_p(\mathbf{r},\mathbf{n})}. \tag{3.49}$$

Inserting all these new functions into eqs.(3.43) gives the potential for a prolate spheroid whose symmetry axis is given by the arbitrary unit vector $\mathbf{n}$:

$$\begin{aligned} \Phi_{r1}(x,y,z) &= (\mathbf{H}_0\cdot\mathbf{r})\,L_1\,(\bar{f}_1-\bar{f}_2)\;+ \\ &\quad+\;(\mathbf{H}_0\cdot\mathbf{n})(\mathbf{n}\cdot\mathbf{r})\,[L_0\,(\bar{f}_1-\bar{f}_3)\;-\;L_1\,(\bar{f}_1-\bar{f}_2)], \end{aligned} \tag{3.50}$$

$$\Phi_{r2}(x,y,z) \;=\; (\mathbf{H}_0\cdot\mathbf{r})\,(M_1+1)\;+\;(\mathbf{H}_0\cdot\mathbf{n})(\mathbf{n}\cdot\mathbf{r})\,[M_0\;-\;M_1]. \tag{3.51}$$

The evaluation of the magnetic field requires the gradients of the functions $\bar{f}_i$. These are done by symbolic computation. Since the resulting expressions consist again of polynomials and the square roots already occuring in the potential it is possible to find simpler expressions. These are again checked against the original gradients by symbolic computation (notebook ProlPotDerivatives.nb [2]). All gradients are proportional to the vector $\mathbf{r}_p$:

$$\mathbf{r}_p \;:=\; \frac{\sqrt{2}}{e_p^2}\left(\mathbf{r} - 2\mathbf{n}\,\frac{(\mathbf{n}\cdot\mathbf{r})}{[\bar{u}_p(\mathbf{r},\mathbf{n})]^2}\right). \tag{3.52}$$

$$\nabla\bar{f}_1 \;=\; \frac{\bar{u}_p(\mathbf{r},\mathbf{n})}{[2-(\bar{u}_p(\mathbf{r},\mathbf{n}))^2]\bar{w}_p(\mathbf{r},\mathbf{n})}\,\mathbf{r}_p, \tag{3.53}$$

$$\nabla\bar{f}_2 \;=\; -\,\frac{\bar{u}_p(\mathbf{r},\mathbf{n})}{\bar{w}_p(\mathbf{r},\mathbf{n})}\,\frac{(\bar{u}_p(\mathbf{r},\mathbf{n}))^2+2}{[(\bar{u}_p(\mathbf{r},\mathbf{n}))^2-2]^2}\,\mathbf{r}_p, \tag{3.54}$$

$$\nabla\bar{f}_3 \;=\; -\,\frac{1}{\bar{u}_p(\mathbf{r},\mathbf{n})\;\bar{w}_p(\mathbf{r},\mathbf{n})}\,\mathbf{r}_p; \tag{3.55}$$

$$\nabla\bar{f}_1-\nabla\bar{f}_2 \;=\; \frac{\bar{u}_p(\mathbf{r},\mathbf{n})}{\bar{w}_p(\mathbf{r},\mathbf{n})}\,\frac{4}{[(\bar{u}_p(\mathbf{r},\mathbf{n}))^2-2]^2}\,\mathbf{r}_p, \tag{3.56}$$

$$\nabla\bar{f}_1-\nabla\bar{f}_3 \;=\; \frac{2}{[2-(\bar{u}_p(\mathbf{r},\mathbf{n}))^2]\;\bar{u}_p(\mathbf{r},\mathbf{n})\;\bar{w}_p(\mathbf{r},\mathbf{n})}\,\mathbf{r}_p. \tag{3.57}$$

The corresponding checks are contained in the notebook ProlatePotDerivatives.nb.

The vector $\mathbf{r}_p$ and all the gradients listed above are well-defined and real in the exterior of the spheroid, including the interface, where $\eta \geq \eta_p$, which is equivalent with the condition (3.61) in Cartesian coordinates. In fact, a more detailed analysis shows that on the interface:

$$\bar{u}_p(\mathbf{r},\mathbf{n}) \;=\; \sqrt{2}\;\cosh\eta_p, \tag{3.58}$$

$$\bar{w}_p(\mathbf{r},\mathbf{n}) \;=\; \sqrt{z^4/\left(e_p\;\cosh(\eta_p)\right)^4 \;-\; 2z^2/e_p^2 \;+\; \cosh^4\eta_p} \tag{3.59}$$

$$\sinh^2\eta_p \leq \bar{w}_p(\mathbf{r},\mathbf{n}) \leq \cosh^2\eta_p. \tag{3.60}$$

For a $=1$, c $=2$, ($e_p=\sqrt{3}$) one finds $\sqrt{2}\;\cosh\eta_p = 2\sqrt{2/3} = 1.63... > \sqrt{2}$; $1/3 \leq \bar{w}_p(\mathbf{r},\mathbf{n}) \leq 4/3$. For this case the surfaces $u_p(\mathbf{r},\mathbf{e}_z)$ and $w_p(\mathbf{r},\mathbf{e}_z)$ are shown in Figs.3.1 and 3.2 at the end of this chapter.

3.4 Final formulas for the field

So the final formulas for the reaction field excited in an arbitray homogeneous primary field $\mathbf{H}_0$ by a prolate spheroid with arbitrary symmetry axis given by a unit vector $\mathbf{n}$ is in the exterior:

$$\frac{r^2 - (\mathbf{n}\cdot\mathbf{r})^2}{a_p^2} + \frac{(\mathbf{n}\cdot\mathbf{r})^2}{c_p^2} \geq 1 \ : \tag{3.61}$$

$$\begin{aligned}
\mathbf{H}_{r1}(x,y,z) \ = \ & - \mathbf{H}_0 \ L_1 \ (\bar{f}_1 - \bar{f}_2) \ - \ \mathbf{n}(\mathbf{H}_0\cdot\mathbf{n})[L_0 \ (\bar{f}_1 - \bar{f}_3) \ - \ L_1 \ (\bar{f}_1 - \bar{f}_2)] \\
& - \mathbf{r}_p \ (\mathbf{H}_0\cdot\mathbf{r}) \ L_1 \ \frac{\bar{u}_p(\mathbf{r},\mathbf{n})}{\bar{w}_p(\mathbf{r},\mathbf{n})} \ \frac{4}{[(\bar{u}_p(\mathbf{r},\mathbf{n}))^2 - 2]^2} \\
& - \mathbf{r}_p \ (\mathbf{H}_0\cdot\mathbf{n})(\mathbf{r}\cdot\mathbf{n}) \ L_0 \ \frac{2}{[2 - (\bar{u}_p(\mathbf{r},\mathbf{n}))^2]\bar{u}_p(\mathbf{r},\mathbf{n}) \ \bar{w}_p(\mathbf{r},\mathbf{n})} \\
& + \mathbf{r}_p \ (\mathbf{H}_0\cdot\mathbf{n})(\mathbf{r}\cdot\mathbf{n}) \ L_1 \ \frac{4 \ \bar{u}_p(\mathbf{r},\mathbf{n})}{\bar{w}_p(\mathbf{r},\mathbf{n}) \ [(\bar{u}_p(\mathbf{r},\mathbf{n}))^2 - 2]^2};
\end{aligned} \tag{3.62}$$

and in the interior:

$$\frac{r^2 - (\mathbf{n}\cdot\mathbf{r})^2}{a_p^2} + \frac{(\mathbf{n}\cdot\mathbf{r})^2}{c_p^2} \leq 1 \ :$$

$$\mathbf{H}_{r2}(x,y,z) \ = \ - \mathbf{H}_0 \ (M_1 + 1) \ - \ \mathbf{n} \ (\mathbf{H}_0\cdot\mathbf{n}) \ [M_0 \ - \ M_1]. \tag{3.63}$$

3.5 Concluding remarks for the field of the prolate spheroid

A prolate spheroid is inserted into an external homogeneous magnetic field $\mathbf{H}_0$ of arbitrary direction. Its susceptibility is $\mu_2 = \mu_0(1+\chi_2)$; while that of the surrounding medium is $\mu_1 = \mu_0(1+\chi_1)$. The spheroid has semi-axes $a_p, a_p, c_p, \ c_p > a_p$; these determine the excentricy e_p and the quasi-radial parameter η_p, eqs.(3.4) and (3.6). These in turn determine the coefficients L_0, L_1, M_0, M_1, eqs.(3.20) to (3.23) or eqs.(3.25) to (3.28). The spheroid's symmetry axis is the arbitrary unit vector $\mathbf{n}$. The reaction field due to the presence of the spheroid in the external field is given in Cartesian coordinates, $\mathbf{r} = (x,y,z)$, by eq.(3.62) in the exterior, by eq.(3.63) in the interior. The functions $\bar{f}_1, \bar{f}_2, \bar{f}_3$, eqs.(3.47) to (3.49), depend on the variables $\bar{u}_p(\mathbf{r},\mathbf{n})$ and $\bar{w}_p(\mathbf{r},\mathbf{n})$, eqs.(3.45) and (3.46). The needed gradients of the $\bar{f}_i$ are given in eqs.(3.56) and (3.57) . Eqs.(3.62) and eq.(3.63) are for a spheroid, whose centre is at the origin. If the centre is at the point $\mathbf{r}_0 = (x_0, y_0, z_0)$ then the vector $\mathbf{r}$ must replaced simply with $\mathbf{r} - \mathbf{r}_0$.

3.6 Figures

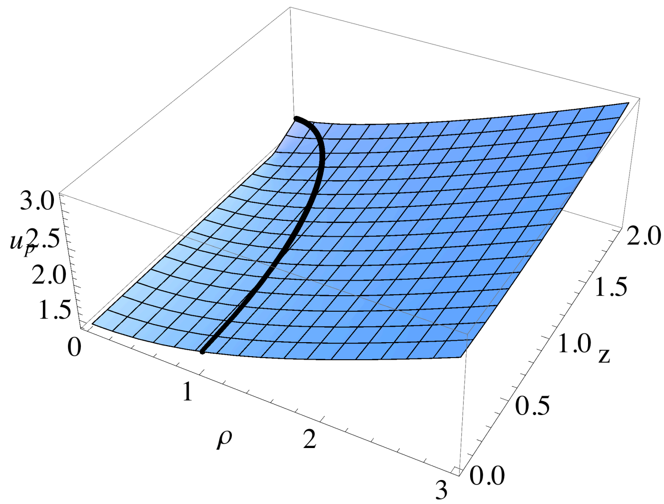

Figure 3.1: The surface $u_p(\mathbf{r}, \mathbf{e}_z)$ as function of the transversal coordinate ρ and the coordinate z along the symmetry axis $\mathbf{e}_z$ for a prolate spheroid with a $=1$, c $=2$; $e_p = \sqrt{3}$. The curve gives the projection of the boundary ellipse $\eta = \eta_p =$ 0.549... (an ellipse in the variables ρ and z) on the surface $u_p(\mathbf{r}, \mathbf{e}_z)$. Points in the exterior of this spheroid correspond to points to the right of the curve on the surface.

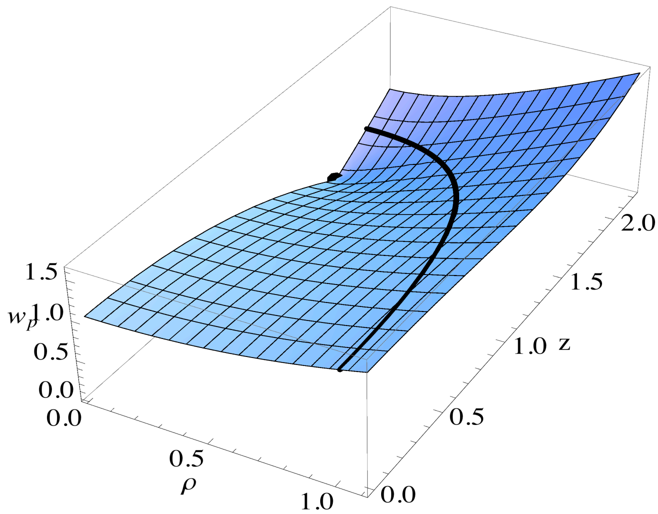

Figure 3.2: The surface $w_p(\mathbf{r}, \mathbf{e}_z)$ as function of the transversal coordinate ρ and the coordinate z along the symmetry axis $\mathbf{e}_z$ for a prolate spheroid with a $=1$, c $=2$; $e_p = \sqrt{3}$. The curve gives the projection of the boundary spheroid $\eta = \eta_p =$ 0.549... (an ellipse in the variables ρ and z) on the surface $w_p(\mathbf{r}, \mathbf{e}_z)$. The point gives the minimum of the surface. Points in the exterior of this spheroid correspond to points to the right of the curve on the surface.

4 A Single Oblate Spheroid in a Homogeneous Magnetic Field

An oblate spheroid (semi-axes $a_o, a_o, c_o;\ c_o < a_o$) with magnetic susceptibility $\mu_2 = \mu_0(1+\chi_2)$ is in a medium with magnetic susceptibility $\mu_1 = \mu_0(1+\chi_1)$ and in an external field (2.1). The solution of this boundary value problem has been sketched in ref. [1]. We use a notation for the coefficients which differs somewhat from that employed in this ref.[1]. The derivations are quite analogous to those used in the previous chapter. The main difference is the different analytical form of the quasi-radial particular solutions.

4.1 The reaction field in oblate spheroidal coordinates

The spheroid induces a reaction field represented by the potentials $\Phi_{r1}(x, y, z)$ in the exterior, by $\Phi_{r2}(x, y, z)$ in the interior. This problem has been solved in ref.[1] in oblate spheroidal coordinates (s., for example, Fig.1.07 of ref.[3])

$$x = e_o\ \cosh\eta\ \sin\theta\ \cos\psi, \tag{4.1}$$

$$y = e_o\ \cosh\eta\ \sin\theta\ \sin\psi, \tag{4.2}$$

$$z = e_o\ \sinh\eta\ \cos\theta; \tag{4.3}$$

$$e_o = \sqrt{a_o^2 - c_o^2} \tag{4.4}$$

for a spheroid, whose symmetry axis coincides with the z-axis. $\Phi_0,\ \Phi_1 = \Phi_0 + \Phi_{r1},\ \Phi_2 = \Phi_0 +\ \Phi_{r2}$ must be solutions of the potential equation in oblate coordinates. This partial differential equation can be solved by separation. The particular solutions of the separated equations suitable for the problem under investigation are Legendre polynomials or functions in $i \sinh\eta$; Legendre polynomials in $\cos\theta$; trigonometric functions in ψ.

The interface separating the two domains is the spheroid:

$$\frac{x^2}{a_o^2} + \frac{y^2}{a_o^2} + \frac{z^2}{c_o^2} = 1 \quad \Leftrightarrow \quad \eta = \eta_o = \mathrm{Artanh}(c_o/a_o). \tag{4.5}$$

The potential and the normal component of the magnetic induction must be continuous across this interface. So conditions (3.7) and (3.8) apply again.

One starts with expansions in the particular solutions fulfilling the boundary conditions. We already know from the previous chapter that only the parameter values n = 1, m = 0 and 1 are needed.

$\eta \geq \eta_o$:

$$
\begin{aligned}
\Phi_1 \;=\;& \; i\; e_o\; H_{0z}\; P_1^0(i \sinh\eta)\; P_1^0(\cos\theta)\; - \\
&- i\; e_o\; (H_{0x}\;\cos\psi + H_{0y}\;\sin\psi)\; P_1^1(i\sinh\eta)\; P_1^1(\cos\theta)\; + \\
&+ \sum_{m=0}^{1}\; {}_1A_1^m\; Q_1^m(i\;\sinh\eta) P_1^m(\cos\theta)\cos(m\psi)\; + \\
&+ {}_1B_1^1\; Q_1^1(i\;\sinh\eta) P_1^1(\cos\theta)\sin\psi\; ; \qquad (4.6)
\end{aligned}
$$

$\eta \leq \eta_o$:

$$
\begin{aligned}
\Phi_2 \;=\;& \sum_{m=0}^{1}\; i\; {}_2A_1^m\; P_1^m(i\sinh\eta) P_1^m(\cos\theta)\cos(m\psi)\; + \\
&+ \;\; i\; {}_2B_1^1\; P_1^1(i\sinh\eta) P_1^1(\cos\theta)\sin\psi\; . \qquad (4.7)
\end{aligned}
$$

We want to get real expansion coefficients. According to ref.[1] eqs.(A64) the $P_1^m(i\sinh\eta)$ are purely imaginary, the $Q_1^m(i\sinh\eta)$ are real. These reality properties are taken into account in inserting the imaginary units in the above expansions for the potentials. The sums are inserted into the continuity conditions (3.7) and (3.8). In view of the orthogonality of the Legendre polynomials $P_n^m(\cos\theta)$ and of the trigonometric functions these two conditions involving sums are decomposed into three independent systems with the solutions:

$$
\begin{aligned}
{}_1A_1^0 \;&=\; i\;\frac{e_o\; H_{0z}\; (\mu_1 - \mu_2)\; P_1^0\; P_1^{0'}}{\mu_2\; P_1^{0'}\; Q_1^0\; -\; \mu_1\; P_1^0\; Q_1^{0'}} \\
&:=\; e_o\; H_{0z}\; \bar{L}_0, \qquad (4.8) \\
{}_2A_1^0 \;&=\; e_o\; H_{0z}\; \mu_1\; \left(\frac{P_1^{0'}\; Q_1^0\; -\; P_1^0\; Q_1^{0'}}{\mu_2\; P_1^{0'}\; Q_1^0\; -\; \mu_1\; P_1^0\; Q_1^{0'}}\right) \\
&:=\; e_o\; H_{0z}\; \bar{M}_0; \qquad (4.9) \\
{}_1A_1^1 \;&=\; i\;\frac{e_o\; H_{0x}\; (\mu_1 - \mu_2)\; P_1^1\; P_1^{1'}}{\mu_2\; P_1^{1'}\; Q_1^1\; -\; \mu_1\; P_1^1\; Q_1^{1'}} \\
&:=\; e_o\; H_{0x}\; \bar{L}_1\; , \qquad (4.10) \\
{}_1B_1^1 \;&=\; e_o\; H_{0y}\; \bar{L}_1, \qquad (4.11) \\
{}_2A_1^1 \;&=\; e_o\; H_{0x}\; \mu_1\; \left(\frac{P_1^{1'}\; Q_1^1\; -\; P_1^1\; Q_1^{1'}}{\mu_2\; P_1^{1'}\; Q_1^1\; -\; \mu_1\; P_1^1\; Q_1^{1'}}\right) \\
&:=\; e_o\; H_{0x}\; \bar{M}_1\; , \qquad (4.12) \\
{}_2B_1^1 \;&=\; e_o\; H_{0y}\; \bar{M}_1\; . \qquad (4.13)
\end{aligned}
$$

The solutions above and further transformations shown below are given in the notebook OblateCoefficientsRev.nb [2]. The argument of all the Legendre polynomials and functions in all of the above equations is $i\sinh\eta_o$. In ref.[1], (A59), (A60) and (A64), it has been shown that the Legendre functions and polynomials may be replaced with elementary functions. So one gets:

$$\begin{aligned}
&\eta \geq \eta_o : \\
&\quad \Phi_{r1} = e_o\,(H_{0x}\ \cos\psi + H_{0y}\ \sin\psi) \times \\
&\qquad \times\ \bar{L}_1\,(\cosh\eta\ \mathrm{arccot}(\sinh\eta) - \tanh\eta)\sin\theta \\
&\qquad +\ e_o\ H_{0z}\ \bar{L}_0\ \ (\sinh\eta\ \mathrm{arccot}(\sinh\eta) - 1)\cos\theta\ , \qquad (4.14)\\
&\eta \leq \eta_o : \\
&\quad \Phi_{r2} = -\ e_o\ (\bar{M}_1 - 1)\ (H_{0x}\ \cos\psi + H_{0y}\ \sin\psi)\ \cosh\eta\ \sin\theta \\
&\qquad -\ e_o\ (\bar{M}_0 - 1)\ H_{0z}\ \sinh\eta\ \cos\theta. \qquad (4.15)
\end{aligned}$$

Making the same substitutions as above in the definitions of the constants $\bar{L}_0, \bar{L}_1, \bar{M}_0, \bar{M}_1$ and going over to the susceptibilities the expressions for the constants become:

$$\bar{L}_0 = L_0^o = \frac{(\chi_1 - \chi_2)\sinh\eta_o}{(1+\chi_2) - (1+\chi_1)\ \tanh^2\eta_o\ +\ (\chi_1 - \chi_2)\ \sinh\eta_o\ \mathrm{arccot}(\sinh\eta_o)}, \qquad (4.16)$$

$$\bar{L}_1 = L_1^o = -\ \frac{(\chi_1 - \chi_2)\ \cosh^2\eta_o\ \sinh\eta_o}{2 + \chi_1 + \chi_2 + (\chi_1 - \chi_2)\ \cosh^2\eta_o\ \left(1 - \sinh\eta_o\ \mathrm{arccot}(\sinh\eta_o)\right)}, \qquad (4.17)$$

$$\bar{M}_0 = M_0^o = \frac{(1+\chi_1)\ \mathrm{sech}^2\eta_o}{(1+\chi_2) - (1+\chi_1)\ \tanh^2\eta_o\ +\ (\chi_1 - \chi_2)\ \sinh\eta_o\ \mathrm{arccot}(\sinh\eta_o)}, \qquad (4.18)$$

$$\bar{M}_1 = M_1^o = \frac{2(1+\chi_1)}{2 + \chi_1 + \chi_2 + (\chi_1 - \chi_2)\ \cosh^2\eta_o\ \left(1 - \sinh\eta_o\ \mathrm{arccot}(\sinh\eta_o)\right)}. \qquad (4.19)$$

The various functions depending on η_o may be replaced by expressions depending only on the semi-axes a_o, c_o.The necessary relations are found from the coordinate transformations (4.1) to (4.4):

$$\begin{array}{lcllcl}
\sinh(\eta_o) & \rightarrow & c_o/e_o, & \cosh(\eta_o) & \rightarrow & a_o/e_o, \\
\tanh(\eta_o) & \rightarrow & c_o/a_o, & \mathrm{arccot}(\sinh\eta_o) & = & \mathrm{arccot}(c_o/e_o) := d_o.
\end{array} \qquad (4.20)$$

The corresponding transformations are given in the notebook OblateCoefficientsRev.nb. Inserting these substitutions and the abbreviation d_o into eqs.(4.16) to(4.19) gives:

$$\begin{aligned}
L_0^o &= [(\chi_1 - \chi_2)c_o/e_o]/D_0^o, && (4.21)\\
D_0^o &= (1+\chi_2) - (1+\chi_1)\ c_o^2/a_o^2\ +\ (\chi_1 - \chi_2)\ d_o c_o/e_o; \\
L_1^o &= -\ [(\chi_1 - \chi_2)\ a_o^2 c_o/e_o^3]/D_1^o, && (4.22)\\
D_1^o &= (2 + \chi_1 + \chi_2)\ +\ (\chi_1 - \chi_2)\ (a_o^2/e_o^2)\ (1 - d_o c_o/e_o). \\
M_0^o &= [(1+\chi_1)\ e_o^2/a_o^2]/D_0^o, && (4.23)\\
M_1^o &= [2(1+\chi_1)]/D_1^o. && (4.24)\\
d_o &= \mathrm{arccot}(c_o/e_o). && (4.25)
\end{aligned}$$

Inserting the expressions above into the reaction potentials Φ_{r1} and Φ_{r2}, these may be rewritten as:

$$\Phi_{1r}(x,y,z) = \big(H_{0x}\,x + H_{0y}\,y\big)\bar{L}_1(g_1-g_2) + H_{0z}\,z\,\bar{L}_0(g_1-g_3), \quad (4.26)$$
$$\Phi_{2r}(x,y,z) = \big(H_{0x}\,x + H_{0y}\,y\big)(1-\bar{M}_1) + H_{0z}\,z\,(1-\bar{M}_0). \quad (4.27)$$

The functions g_1, g_2, g_3 depend solely on the function $\sinh\eta$:

$$g_1 = \operatorname{arccot}(\sinh\eta), \quad (4.28)$$
$$g_2 = \frac{\sinh\eta}{\cosh^2\eta}, \quad (4.29)$$
$$g_3 = \frac{1}{\sinh\eta}. \quad (4.30)$$

If both media are the same both reaction potentials must be zero. Indeed, the limits of the four coefficients

$$\chi_2 \rightarrow \chi_1 : \quad \bar{L}_0 \rightarrow 0,\ \bar{L}_1 \rightarrow 0,\ \bar{M}_0 \rightarrow 1,\ \bar{M}_1 \rightarrow 1 \quad (4.31)$$

ensure this.

4.2 The reaction field in Cartesian coordinates

We want expressions for the potential which depend on x, y, z only. So $\sinh\eta$ must be replaced with a corresponding expression in Cartesian coordinates. From eqs.(4.1) to (4.3) one finds:

$$\sinh^2\eta = \frac{1}{2}\left(-1+\frac{r^2}{e_o^2} \pm \sqrt{\left(-1+\frac{r^2}{e_o^2}\right)^2 + 4\frac{z^2}{e_o^2}}\right).$$

Since the square root is larger than the preceeding polynomial it is obvious that only the plus sign applies. This is also confirmed by intense numerical studies. So we have:

$$\sinh\eta = \frac{1}{\sqrt{2}}\sqrt{-1+\frac{r^2}{e_o^2}+w_o(\mathbf{r},\mathbf{e}_z)} := u_o(\mathbf{r},\mathbf{e}_z)/\sqrt{2}, \quad (4.32)$$

$$w_o(\mathbf{r},\mathbf{e}_z) = \sqrt{\left(-1+\frac{r^2}{e_o^2}\right)^2 + 4\frac{z^2}{e_o^2}} = \sqrt{\left(-1+\frac{r^2}{e_o^2}\right)^2 + 4\frac{(\mathbf{r}\cdot\mathbf{e}_z)^2}{e_o^2}}, \quad (4.33)$$

$$r^2 = x^2+y^2+z^2. \quad (4.34)$$

Inserting this expression for $\sinh\eta$ into eqs.(4.28) to (4.30) and inserting the resulting expressions for g_1, g_2, g_3

$$g_1 = \operatorname{arccot}(u_o(\mathbf{r}, \mathbf{e}_z)/\sqrt{2}), \tag{4.35}$$

$$g_2 = \frac{\sqrt{2}\; u_o(\mathbf{r}, \mathbf{e}_z)}{[u_o(\mathbf{r}, \mathbf{e}_z)]^2 + 2}, \tag{4.36}$$

$$g_3 = \frac{\sqrt{2}}{u_o(\mathbf{r}, \mathbf{e}_z)}. \tag{4.37}$$

into eq.(4.26) we get the final expression for the exterior potential as pure function of the Cartesian coordinates x, y, z:

$$\Phi_{r1}(x, y, z) = (H_{0x}\; x\; + H_{0y}\; y)\; \bar{L}_1\; (g_1 - g_2)\; +\; H_{0z}\; z\; \bar{L}_0\; (g_1 - g_3). \tag{4.38}$$

The interior potential, eq.(4.27), is already a pure function of the Cartesian coordinates.

4.3 Potential and field for an arbitrary direction of the spheroidal symmetry axis

For applications it is necessary to consider spheroids whose symmetry axis has an arbitrary direction. The corresponding expressions for the potential will be derived from those given in eqs.(4.38) and (4.27). These are rewritten in a way suggesting a general form:

$$\Phi_{r1}(x, y, z) = (\mathbf{H}_{0\perp} \cdot \mathbf{r}_\perp)\; \bar{L}_1\; (g_1 - g_2)\; +\; (\mathbf{H}_{0\parallel} \cdot \mathbf{r}_\parallel)\; \bar{L}_0\; (g_1 - g_3), \tag{4.39}$$

$$\Phi_{r2}(x, y, z) = (\mathbf{H}_{0\perp} \cdot \mathbf{r}_\perp)\; (1 - \bar{M}_1)\; +\; (\mathbf{H}_{0\parallel} \cdot \mathbf{r}_\parallel)(1 - \bar{M}_0). \tag{4.40}$$

The vectors $\mathbf{H}_{0\parallel}, \mathbf{r}_\parallel$ give the projections of the corresponding vectors on the symmetry axis, i.e. the z-axis. Similarly, the vectors $\mathbf{H}_{0\perp} = (H_{0x}, H_{0y}, 0)$, $\mathbf{r}_\perp = (x, y, 0)$ give the projection of the corresponding vectors onto the x,y-plane, which is perpendicular to the symmetry axis. Now it is easy to accomplish the substitutions for an arbitrary position of the symmetry axis given by the unit vector $\mathbf{n}$ as given in eqs.(3.44)

In w_o, eq.(4.33), only the variable z, the component of the position vector along the z-Axis, i.e. the symmetry axis, must be replaced by $(\mathbf{n} \cdot \mathbf{r})$ giving:

$$\sinh \eta = \frac{1}{\sqrt{2}} \sqrt{-1 + \frac{r^2}{e_o^2} + \bar{w}_o(\mathbf{r}, \mathbf{n})} \;:=\; \bar{u}_o(\mathbf{r}, \mathbf{n})/\sqrt{2}, \tag{4.41}$$

$$\bar{w}_o(\mathbf{r}, \mathbf{n}) = \sqrt{\left(-1 + \frac{r^2}{e_o^2}\right)^2 + 4\frac{(\mathbf{n} \cdot \mathbf{r})^2}{e_o^2}}. \tag{4.42}$$

The functions g_i, eqs.(4.35) to (4.37), remain the same except that $u_o(\mathbf{r}, \mathbf{e}_z)$ and $w_o(\mathbf{r}, \mathbf{e}_z)$

must be replaced with $\bar{u}_o(\mathbf{r},\mathbf{n})$ and $\bar{w}_o(\mathbf{r},\mathbf{n})$ giving the new functions $\bar{g}_i$:

$$\bar{g}_1 = \operatorname{arccot}(\bar{u}_o(\mathbf{r},\mathbf{n})/\sqrt{2}), \tag{4.43}$$

$$\bar{g}_2 = \frac{\sqrt{2}\ \bar{u}_o(\mathbf{r},\mathbf{n})}{[\bar{u}_o(\mathbf{r},\mathbf{n})]^2+2}, \tag{4.44}$$

$$\bar{g}_3 = \frac{\sqrt{2}}{\bar{u}_o(\mathbf{r},\mathbf{n})}. \tag{4.45}$$

Inserting all these new functions into eqs.(4.40) gives the potential for an oblate spheroid whose symmetry axis is given by the arbitrary unit vector $\mathbf{n}$:

$$\Phi_{r1}(x,y,z) = (\mathbf{H}_0\cdot\mathbf{r})\ \bar{L}_1\ (\bar{g}_1-\bar{g}_2)\ + \tag{4.46}$$

$$+\ (\mathbf{H}_0\cdot\mathbf{n})(\mathbf{n}\cdot\mathbf{r})\ [\bar{L}_0\ (\bar{g}_1-\bar{g}_3)\ -\ \bar{L}_1\ (\bar{g}_1-\bar{g}_2)], \tag{4.47}$$

$$\Phi_{r2}(x,y,z) = (\mathbf{H}_0\cdot\mathbf{r})\ (1-\bar{M}_1)\ +\ (\mathbf{H}_0\cdot\mathbf{n})(\mathbf{n}\cdot\mathbf{r})\ [\bar{M}_1\ -\ \bar{M}_0]. \tag{4.48}$$

The evaluation of the magnetic field requires the gradients of the functions $\bar{g}_i$. These are done by symbolic computation (OblPotDerivatives.nb [2]). Since the resulting expressions consist again of polynomials and the square roots already occuring in the potential it is possible to find simpler expressions. These are again checked against the original gradients by symbolic computation. All these derivatives are proportional to the vector $\mathbf{r}_o$

$$\mathbf{r}_o := \frac{\sqrt{2}}{e_o^2}\left(\mathbf{r}\ +\ 2\mathbf{n}\ \frac{(\mathbf{n}\cdot\mathbf{r})}{(\bar{u}_o(\mathbf{r},\mathbf{n}))^2}\right). \tag{4.49}$$

$$\nabla\bar{g}_1 = -\ \frac{\bar{u}_o(\mathbf{r},\mathbf{n})}{[2+(\bar{u}_o(\mathbf{r},\mathbf{n}))^2]\bar{w}_o(\mathbf{r},\mathbf{n})}\ \mathbf{r}_o, \tag{4.50}$$

$$\nabla\bar{g}_2 = \frac{\bar{u}_o(\mathbf{r},\mathbf{n})}{\bar{w}_o(\mathbf{r},\mathbf{n})}\ \frac{2-(\bar{u}_o(\mathbf{r},\mathbf{n}))^2}{[(\bar{u}_o(\mathbf{r},\mathbf{n}))^2+2]^2}\ \mathbf{r}_o(\mathbf{r},\mathbf{n}), \tag{4.51}$$

$$\nabla\bar{g}_3 = -\ \frac{1}{\bar{u}_o(\mathbf{r},\mathbf{n})\ \bar{w}_o(\mathbf{r},\mathbf{n})}\ \mathbf{r}_o; \tag{4.52}$$

$$\nabla\bar{g}_1-\nabla\bar{g}_2 = -\ \frac{\bar{u}_o(\mathbf{r},\mathbf{n})}{\bar{w}_o(\mathbf{r},\mathbf{n})}\ \frac{4}{[(\bar{u}_o(\mathbf{r},\mathbf{n}))^2+2]^2}\ \mathbf{r}_o, \tag{4.53}$$

$$\nabla\bar{g}_1-\nabla\bar{g}_3 = \frac{2}{[2+(\bar{u}_o(\mathbf{r},\mathbf{n}))^2]\ \bar{u}_o(\mathbf{r},\mathbf{n})\ \bar{w}_o(\mathbf{r},\mathbf{n})}\ \mathbf{r}_o. \tag{4.54}$$

The corresponding checks are contained in the notebook OblatePotDerivatives.nb.

The vector $\mathbf{r}_o$ and all the gradients listed above are well-defined and real in the exterior of the oblate spheroid, where $\eta \geq \eta_o$; which is equivalent with the condition (4.58) in Cartesian coordinates. In fact, a more detailed analysis shows that on the interface:

$$\bar{u}_o(\mathbf{r},\mathbf{n}) = \sqrt{2}\ \sinh\eta_o, \tag{4.55}$$

$$\bar{w}_o(\mathbf{r},\mathbf{n}) = \sqrt{z^4/\big(e_o\ \sinh(\eta_o)\big)^4\ +\ 2z^2/e_o^2\ +\ \sinh^4\eta_o} \tag{4.56}$$

$$\sinh^2\eta_o \leq \bar{w}_o(\mathbf{r},\mathbf{n}) \leq \cosh^2\eta_o. \tag{4.57}$$

For a = 1, c = 2, ($e_o = \sqrt{3}$) one finds $\sqrt{2}\ \sinh\eta_o = \sqrt{2/3} = 0.816...$; $1/3 \le \bar{w}_o(\mathbf{r},\mathbf{n}) \le 4/3$. For this case the surfaces $u_o(\mathbf{r},\mathbf{e}_z)$ and $w_o(\mathbf{r},\mathbf{e}_z)$ are shown in Figs.4.1 and 4.2 at the end of this chapter.

4.4 Final formulas for the field

So the final formulas for the reaction field excited in an arbitray homogeneous primary field $\mathbf{H}_0$ by an oblate spheroid with arbitrary symmetry axis given by a unit vector $\mathbf{n}$ is in the exterior:

$$\frac{r^2-(\mathbf{n}\cdot\mathbf{r})^2}{a_o^2}+\frac{(\mathbf{n}\cdot\mathbf{r})^2}{c_o^2}\ge 1\ : \tag{4.58}$$

$$\begin{aligned}\mathbf{H}_{r1}(x,y,z) \;=\; & -\,\mathbf{H}_0\ \bar{L}_1\ (\bar{g}_1-\bar{g}_2)\ -\ \mathbf{n}(\mathbf{H}_0\cdot\mathbf{n})[\bar{L}_0\ (\bar{g}_1-\bar{g}_3)\ -\ \bar{L}_1\ (\bar{g}_1-\bar{g}_2)] \\ & +\,\mathbf{r}_o\ (\mathbf{H}_0\cdot\mathbf{r})\ \bar{L}_1\ \frac{\bar{u}_o(\mathbf{r},\mathbf{n})}{\bar{w}_o(\mathbf{r},\mathbf{n})}\ \frac{4}{[2+(\bar{u}_o(\mathbf{r},\mathbf{n}))^2]^2} \\ & -\,\mathbf{r}_o\ (\mathbf{H}_0\cdot\mathbf{n})(\mathbf{r}\cdot\mathbf{n})\ \bar{L}_0\ \frac{2}{[2+(\bar{u}_o(\mathbf{r},\mathbf{n}))^2]\ \bar{u}_o(\mathbf{r},\mathbf{n})\ \bar{w}_o(\mathbf{r},\mathbf{n})} \\ & -\,\mathbf{r}_o\ (\mathbf{H}_0\cdot\mathbf{n})(\mathbf{r}\cdot\mathbf{n})\ \bar{L}_1\ \frac{4\ \bar{u}_o(\mathbf{r},\mathbf{n})}{\bar{w}_o(\mathbf{r},\mathbf{n})\ [(\bar{u}_o(\mathbf{r},\mathbf{n}))^2+2]^2};\end{aligned} \tag{4.59}$$

and in the interior:

$$\frac{r^2-(\mathbf{n}\cdot\mathbf{r})^2}{a_o^2}+\frac{(\mathbf{n}\cdot\mathbf{r})^2}{c_o^2}\le 1\ :$$

$$\mathbf{H}_{r2}(x,y,z) \;=\; \mathbf{H}_0\ (1-\bar{M}_1)\ +\ \mathbf{n}\ (\mathbf{H}_0\cdot\mathbf{n})\ [\bar{M}_1\ -\ \bar{M}_0]. \tag{4.60}$$

4.5 Concluding remarks for the field of an oblate spheroid

An oblate spheroid is inserted into an external homogeneous magnetic field $\mathbf{H}_0$ of arbitrary direction. Its susceptibility is $\mu_2 = \mu_0(1+\chi_2)$; while that of the surrounding medium is $\mu_1 = \mu_0(1+\chi_1)$. The spheroid has semi-axes $a_o, a_o, c_o,\ c_o < a_o$; these determine the excentricy e_o and the quasi-radial parameter η_o, eqs.(4.4) and (4.5). These in turn determine the coefficients $\bar{L}_0, \bar{L}_1, \bar{M}_0, \bar{M}_1$, eqs.(4.16) to (4.19) or eqs.(4.21) to (4.24). The spheroid's symmetry axis is the arbitrary unit vector $\mathbf{n}$. The reaction field due to the presence of the spheroid in the external field is given in Cartesian coordinates, $\mathbf{r} = (x,y,z)$, by eq.(4.59) in the exterior, by eq.(4.60) in the interior. The functions $\bar{g}_1, \bar{g}_2, \bar{g}_3$, eqs.(4.43) to (4.45), depend on the variables $\bar{u}_o(\mathbf{r},\mathbf{n})$ and $\bar{w}_o(\mathbf{r},\mathbf{n})$, eqs.(4.41) and (4.42). The needed gradients of the $\bar{g}_i$ are given in eqs.(4.53) and (4.54) . Eqs.(4.59) and eq.(4.60) are for a spheroid, whose centre is at the origin. If the centre is at the point $\mathbf{r}_0 = (x_0, y_0, z_0)$ then the vector $\mathbf{r}$ must replaced simply with $\mathbf{r}-\mathbf{r}_0$.

4.6 Figures

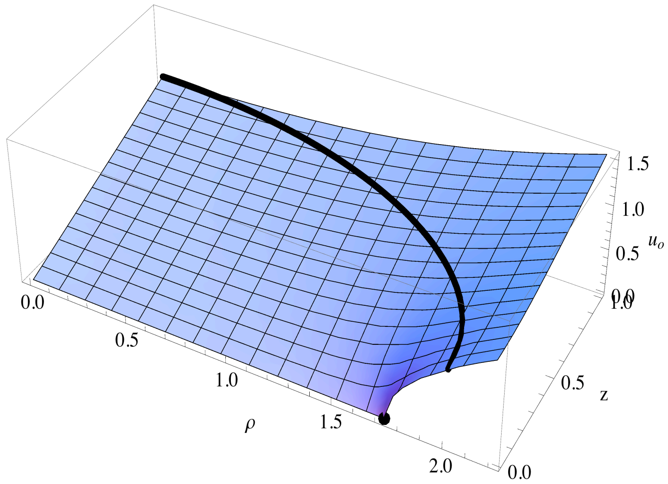

Figure 4.1: The surface $u_o(\mathbf{r}, \mathbf{e}_z)$ as function of the transversal coordinate ρ and the coordinate z along the symmetry axis $\mathbf{e}_z$ for an oblate spheroid with a = 2, c = 1; $e_o = \sqrt{3}$. The curve gives the projection of the boundary spheroid $\eta = \eta_o =$ 0.549306 (an ellipse in the variables ρ and z) on the surface $u_o(\mathbf{r}, \mathbf{e}_z)$. Points in the exterior of this spheroid correspond to points to the right of the curve on the surface.

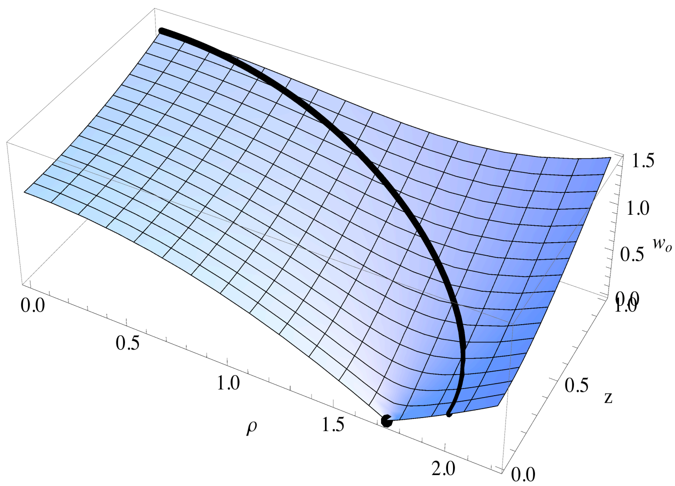

Figure 4.2: The surface $w_o(\mathbf{r}, \mathbf{e}_z)$ as function of the transversal coordinate ρ and the coordinate z along the symmetry axis $\mathbf{e}_z$ of an oblate spheroid with a = 2, c = 1; $e_o = \sqrt{3}$. The curve gives the projection of the boundary spheroid $\eta = \eta_o =$ 0.549306 (an ellipse in the variables ρ and z) on the surface $w_o(\mathbf{r}, \mathbf{e}_z)$. Points in the exterior of this ellipse correspond to points to the right of the curve on the surface.

5 Tensors for the Reaction Fields

Inserting a prolate or oblate spheroid into the primary homogeneous magnetic field produces a reaction field within and near the spheroid. This reaction may be represented by a tensor transforming the primary field into the reaction field. We succeeded in preparing formulas representing these tensors in a very concise way. In a way this is just a rewriting the formulas given in the previous two chapters. But this shows the similarities between the formulas for the prolate and the oblate case more clearly.

The values η_p, η_o respectively determining the boundaries of the spheroids are the same as defined in eqs.(3.6), (4.5) respectively.

$$\eta_p = \mathrm{Arcoth}(c_p/a_p), \tag{5.1}$$

$$\eta_o = \mathrm{Artanh}(c_o/a_o). \tag{5.2}$$

5.1 The potentials of the reaction fields

The presence of a spheroid induces a reaction field with potential ($\mathbf{r} = (x_\beta)$) :

$$\Phi_k^\sigma(x,y,z) = \sum_{\alpha,\beta=1}^{3} H_{0\alpha} t_{\alpha\beta}^{\sigma,k} x_\beta = \mathbf{H}_0 \cdot \mathbf{T}^{\sigma,k} \cdot \mathbf{r} \tag{5.3}$$

with $\sigma = p$ (= prolate) or $= o$ (= oblate) and k = e (= external) or i (= internal) to the ellipsoid

$$\mathcal{E}_\sigma := \frac{r^2 - (\mathbf{n}\cdot\mathbf{r})^2}{a_\sigma^2} + \frac{(\mathbf{n}\cdot\mathbf{r})^2}{c_\sigma^2} = 1. \tag{5.4}$$

For a prolate spheroid, $a_p < c_p$, the excentricity is $e_p = \sqrt{c_p^2 - a_p^2}$; for an oblate one, $c_o < a_o$, and the excentricity is $e_o = \sqrt{a_o^2 - c_o^2}$.

5.1.1 The coefficients $L_0^\sigma, L_1^\sigma, M_0^\sigma, M_1^\sigma$

The coefficients $L_0^\sigma, L_1^\sigma, M_0^\sigma, M_1^\sigma$ depend only on the geometric shape of the spheroids, i.e. on η_σ or on the semi-axes a_σ, c_σ, and on the magnetic susceptibilites χ_1, χ_2. These constant parameters determine the coefficients $L_0^\sigma, L_1^\sigma, M_0^\sigma, M_1^\sigma$. The corresponding formulas have been given in eqs.(3.20) to (3.23) (or (3.25) to (3.28)) for the prolate case and in eqs.(4.16) to (4.19) (or (4.21) to (4.24)) for the oblate case.

5.1.2 The tensors for the scalar potential of the reaction

In the exterior, $\mathcal{E}_\sigma \geq, 1$ the tensor $\mathbf{T}^{e,\sigma} = (T^{e,\sigma}_{\alpha\beta})$ is:

$$T^{e,\sigma}_{\alpha\beta} \;=\; \delta_{\alpha\beta}\, L^\sigma_1\,(f^\sigma_1 - f^\sigma_2) \;+\; n_\alpha n_\beta [L^\sigma_0\,(f^\sigma_1 - f^\sigma_3) - L^\sigma_1\,(f^\sigma_1 - f^\sigma_2)]. \tag{5.5}$$

This formula is the concise presentations of eqs.(3.62), eqs.(4.59) respectively.
In the interior, $\mathcal{E}_\sigma \leq 1$, the field is homogeneous:

$$T^{i,\sigma}_{\alpha\beta} = \delta_{\alpha\beta}\,(1 \pm M^\sigma_1) \pm\; n_\alpha n_\beta\,(M^\sigma_0 - M^\sigma_1). \tag{5.6}$$

This formula is the concise presentations of eqs.(3.63), eqs.(4.60) respectively.
Above and below the upper (lower) signs apply for $\sigma =$ p (o).

$$\begin{aligned}
f^p_1 &= \operatorname{Arcoth}\big(u_p(\mathbf{n},\mathbf{r})/\sqrt{2}\big) && (5.7)\\
f^o_1 &= \operatorname{arccot}\big(u_o(\mathbf{n},\mathbf{r})/\sqrt{2}\big) && (5.8)\\
f^\sigma_2 &= \sqrt{2}\; u_\sigma(\mathbf{n},\mathbf{r})/[\big(u_\sigma(\mathbf{n},\mathbf{r})\big)^2 \mp 2] && (5.9)\\
f^\sigma_3 &= \sqrt{2}/u_\sigma(\mathbf{n},\mathbf{r}) && (5.10)\\
u_{p,o}(\mathbf{n},\mathbf{r}) &= \sqrt{\pm 1 + r^2/e^2_{p,o} \;+\; w_{p,o}(\mathbf{n},\mathbf{r})} && (5.11)\\
w_{p,o}(\mathbf{n},\mathbf{r}) &= \sqrt{\big(\pm 1 + r^2/e^2_{p,o}\big)^2 \;\mp\; 4(\mathbf{n}\cdot\mathbf{r})^2/e^2_{p,o}}. && (5.12)
\end{aligned}$$

5.2 The magnetic reaction fields

For the evaluation of the signals the magnetic reaction fields are needed. The tensors $\mathbf{K}^{\sigma,k} = (K^{\sigma,k}_{\alpha\beta})$ transform the primary field $\mathbf{H}_0 = (H_{0\beta})$ into the reaction fields $\mathbf{H}^\sigma_k = (H^{\sigma,k}_\alpha)$:

$$H^{\sigma,k}_\alpha(x,y,z) \;=\; \sum_{\beta=1}^{3} K^{\sigma,k}_{\alpha\beta}\; H_{0\beta}, \quad \sigma = p,o; k = e,i. \tag{5.13}$$

The tensors are found in Chapters 3 and 4 by computing the gradients of the reaction potentials. This requires also the gradients of the functions f^σ_n; which are evaluated by symbolic computation [2] using *Mathematica*. Since the resulting expressions consist again of polynomials and the square roots already occuring in the exterior potentials it is possible to find simpler expressions. These are again checked against the original gradients by symbolic computation [2]. All gradients are proportional to the vectors $\mathbf{r}^p(= x^p_\alpha), \mathbf{r}^o(= x^o_\alpha)$ respectively:

$$\mathbf{r}^{p,o} \;:=\; \frac{\sqrt{2}}{e^2_{p,o}}\left(\mathbf{r} \;\mp\; 2\mathbf{n}\,\frac{(\mathbf{n}\cdot\mathbf{r})}{[u_{p,o}(\mathbf{r},\mathbf{n})]^2}\right) \;:=\; (x^\sigma_\alpha). \tag{5.14}$$

The expressions for the reaction tensors of prolate or oblate spheroids with symmetry axis $\mathbf{n}$ in an extermal homogeneous magnetic field $\mathbf{H}_0$ in the exterior are found in eqs.(3.62), (4.59) respectively:

$$\begin{aligned}
\mathcal{E}_\sigma \quad &\geq 1 \quad : \\
K^{\sigma,e}_{\alpha\beta}(x,y,z) \quad &= \quad -\,\delta_{\alpha\beta}\, L^\sigma_1\,(f^\sigma_1 - f^\sigma_2) \;-\; n_\alpha n_\beta\,[L^\sigma_0\,(f^\sigma_1 - f^\sigma_3) \;-\; L^\sigma_1\,(f^\sigma_1 - f^\sigma_2)] \\
&\mp\, x^\sigma_\alpha\, x_\beta\, L^\sigma_1\, \frac{u_\sigma(\mathbf{r},\mathbf{n})}{w_\sigma(\mathbf{r},\mathbf{n})}\, \frac{4}{[(u_\sigma(\mathbf{r},\mathbf{n}))^2 \mp 2]^2} \\
&-\, x^\sigma_\alpha\, n_\beta\, (\mathbf{r}\cdot\mathbf{n})\, L^\sigma_0\, \frac{2}{[2 \mp (u_\sigma(\mathbf{r},\mathbf{n}))^2]u_\sigma(\mathbf{r},\mathbf{n})\; w_\sigma(\mathbf{r},\mathbf{n})} \\
&\pm\, x^\sigma_\alpha\, n_\beta\, (\mathbf{r}\cdot\mathbf{n})\, L^\sigma_1\, \frac{4\, u_\sigma(\mathbf{r},\mathbf{n})}{w_\sigma(\mathbf{r},\mathbf{n})\;[(u_\sigma(\mathbf{r},\mathbf{n}))^2 \mp 2]^2}.
\end{aligned} \tag{5.15}$$

The upper, lower signs respectively apply to prolate ($\sigma = \mathrm{p}$), oblate ($\sigma = \mathrm{o}$) spheroids respectively. The fields in the interior are homogeneous, but are not parallel to the primary field, in general; they are found in eqs.(3.63), (4.60) respectively:

$$\begin{aligned}
\mathcal{E}_\sigma \quad &\leq 1 \quad : \\
K^{\sigma,i}_{\alpha,\beta}(x,y,z) \quad &= \quad -\,\delta_{\alpha\beta}\,(M^\sigma_1 \pm 1) - \; n_\alpha n_\beta\,(M^\sigma_0 - M^\sigma_1).
\end{aligned} \tag{5.16}$$

The theory above has been derived under the assumption that the spheroid is centred at the origin. If the centre is at the point $\mathbf{r}_0$ then $\mathbf{r}$ must be replaced by $\mathbf{r} - \mathbf{r}_0$ in all formulas.

6 Application: Modelling trabecular bone

6.1 Introduction

Generally, in magnetic resonance experiments disturbances of the homogeneous main magnetic field have an essential impact on the formation of the resonance signal. In principle magnetic inhomogeneities can be classified with respect to their origin and strength, and their influence on the formation of the signal decay [6]. Susceptibility effects in MRI/MRS are of great interest. Especially in MR-Osteodensitometry information about the status of cancellous bone can be gained [7, 8]. In the presence of trabeculae the relaxation properties of bone marrow are changed due to the inhomogeneity of the magnetic field, induced by the discontinuities of the magnetic susceptibility across the surface of the bone [9]. In several studies direct relations between the effective transversal relaxation time T_2^* with bone mineral density (BMD) [10, 11, 12] and with mechanical competence of trabecular bone! [13, 14, 15] were reported.

The signal decay in a gradientecho experiment due to additional local field inhomogeneities follows the empirical expression:

$$S(T_E) \propto e^{-R_2^* T_E} \quad \text{with} \quad R_2^* = 1/T_2 + R_2' \,, \tag{6.1}$$

with T_2 giving the intrinsic transversal relaxation time and T_E the echo time. The quantity R_2' accounts for the additional contribution, originating from the local field inhomogeneities, to the effective transversal relaxation rate $R_2^* = 1/T_2^*$. In the simplest case the inhomogeneous magnetic field varies linearly across the sample, thus $R_2' \approx \gamma \Delta B$ with ΔB representing the field variation and γ the gyromagnetic ratio.

Computer simulations modelling the susceptibility induced magnetic field distortion make it possible to gain insight into the interrelationship between the temporal behaviour of the resonance signal caused by histomorphometrical parameters of the spongious microarchitecture. The aim is to analyse effects on the induced line broadening of the resonance spectra evoked through important morphometric quantities such as intertrabecular distance, trabecular thickness and bone volume fraction.

6.2 Modelling: Computersimulation

The evaluation of the magnetic field distribution was performed utilizing a two-compartment model, consisting of bone marrow and the mineralized bone. In a three-dimensional unit cell representing the region of interest the two types of ellipsoids were arranged appropriately to model the known trabecular microstructure [16]. For the simulation of architectures made up by plate-like trabeculae, as they can be found in the epiphysis of long bones like the femur, oblate spheroids were used. For the study of trabecular cracks within a vertebra the unit cell was set up by prolate spheroids.

The developed computer simulations analysing the MR signal evolution are based on an approach described by Bakker et al. [17]. Hence, in a first step the reaction fields induced by the susceptibility difference between the ellipsoids (trabeculae) and the background (bone marrow) were computed. Subsequently a Fourier Transformation of the spatial magnetic field distribution with respect to time yielded the signal curve [18].

The precession frequency of spins in a homogeneous magnetic field is determined through the magnetic induction $\mathbf{B}$. Introducing a sample with a different susceptibility the resulting magnetic induction B_z can be generally written:

$$B_z = \mu \left(H_{0z} + \Delta H_{r1,z}\left(\mathbf{r}\right)\right) = \left(1 + 4\pi\chi\right)\left(H_{0z} + \Delta H_{r1,z}\left(\mathbf{r}\right)\right), \tag{6.2}$$

$\Delta H_{r1,z}$ characterizing the induced reaction field. Further, throughout the simulations the CGS-system was applied, susceptibility units are per unit mass.

The resulting magnetic field distribution within the unit cell was determined as the sum of the individual contributions H_{zi} originating from all ellipsoids n:

$$\Delta H_{r1,z}\left(\mathbf{r}\right) = \sum_{i=1}^{n} H_{zi}\left(\mathbf{r}\right). \tag{6.3}$$

Interactions between the trabeculae have been neglected. This assumption is valid, since interactions between such structures include susceptibility effects of the second order, which will give rise to field contributions of the order of $\mathbf{H}_0\left(\Delta\chi\right)^2$, or $\approx 10^{-6}\ \mathbf{H}_0$.

In a simple MR experiment, excitation followed by an acquisition period, the signal of the free induction decay (FID) can be written as:

$$S(t) = \text{const} \int d^3\mathbf{r}\ e^{-i\omega(\mathbf{r})t}\ e^{-t/T_2}; \tag{6.4}$$

with $\omega(\mathbf{r}) = \gamma B_z(\mathbf{r})$ it follows:

$$S(t) = \text{const} \int d^3\mathbf{r}\ e^{-i\gamma B_z(\mathbf{r})t}\ e^{-t/T_2}. \tag{6.5}$$

Using again expression (6.2) the following expression in $\Delta H_{r1,z}$ can be found:

$$S(t) = \text{const} \int d^3\mathbf{r}\ e^{-i\gamma t(1+4\pi\chi)(H_{0z}+\Delta H_{r1,z}(\mathbf{r}))}\ e^{-t/T_2}. \tag{6.6}$$

This integral must be extended over the entire unit cell enclosing the ellipsoids.

In order to compare the simulation results with MR images the magnitude of $S(t)$ must be found. Except for the dissipative relaxation phenomenon e^{-t/T_2} the expressions in (6.6) are purely oscillatory in H_{0z}. Hence, for the analysis of the signal course the essential decay can be expressed as:

$$|S(t)| = \text{const} \int d^3\mathbf{r}\ e^{-i\gamma t(1+4\pi\chi)\Delta H_{r1,z}(\mathbf{r})}. \tag{6.7}$$

$\Delta H_{r1,z}(\mathbf{r})$ can be computed according to (6.3) as the sum over all the reactions fields of the individual ellipsoids, where $(1 + 4\pi\chi)$ describes the magnetic permeability at the location $\mathbf{r}$.

6.2.1 Algorithm

Utilizing the expressions developed for the reaction fields (3.62) and (4.59) two sets of simulations were implemented in *Mathematica* (Wolfram Research, Inc.). The program computed the field distribution of $\Delta H_{r1,z}(\mathbf{r})$ in the sense of a histogram and generated the MR signal curve according to (6.7).

As input parameters of the simulations the spacing of the trabeculae in x-, y- and z-direction, the dimensions of the ellipsoids and the position of the symmetry axis with respect to the z-axis of the coordinate system had to be defined. Further, the susceptibilities of the bones and the background as well as the orientation of the applied homogenous main magnetic field had to be set. The results of the simulations were the histograms of the magnetic field distribution and the signal curve, which was further utilized within a fitting-procedure yielding the relaxation constant R_2'.

6.2.2 Data fitting

Utilizing the simulated signal curves a Gaussian signal model was applied in order to approximate the relaxation time T_2' [19, 20]. The computed signal intensities (6.7) at the echo times ranging from 0 to 50 ms, 2.5 ms increment, were used to generate a single T_2' value by means of a non linear least-squares-approximation to a three parameter fit function:

$$S(t) = A + B\ e^{-t^2/\left(2T_2'^2\right)}\ . \tag{6.8}$$

The fitting model is equivalent to a bi-Gaussian function with one term having a decay constant greater than the maximum T_E (50 ms). A high value of the ratio A/B corresponds to a decay that deviates significantly from a single Gaussian [21, 20].

6.2.3 Model I

The effect of the loss of bone mass within a three-dimensional plate-like trabecular model was analysed using oblate ellipsoids. Hence, stepwise decreasing of the bone volume fraction $\varsigma = BV/TV$, bone volume (BV)/total volume (TV), was performed. In accordance with the findings of Hildebrand et al. [16], ς values ranging from 0.530–0.406 were investigated. The bone remodelling was simulated through a simultaneously decreasing by 12.5 μm of the thickness of the horizontal and vertical arranged ellipsoids. The external field $\mathbf{H}_0$ was applied setting $\alpha = 5°$ and β parallel to the z-coordinate axis. The configuration of the three-dimensional unit cell and the parameter settings are shown in Fig.6.1 and Tab.6.1-6.2.

6.2.4 Model II

The impact of trabecular cracks on the MR signal evolution was studied using a simple two-dimensional model of vertebrae. Thus, the unit cell was composed out of four prolate ellipsoids, mimicing the initial intact trabeculae. The interruptions were simulated in the

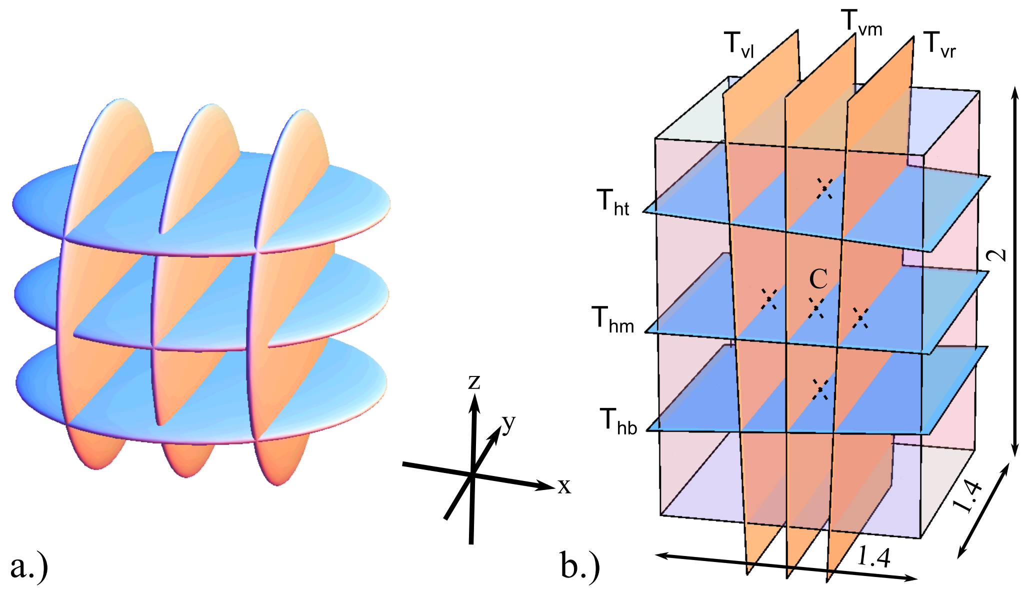

Figure 6.1: a.) Schematic depiction of the six oblate ellipsoids forming the three-dimensional plate-like microstructure of Model I; b.) Detailed view of the applied unit cell, where the dimensions are given in *mm*. The centres of the ellipsoids are indicated by crosses, the subscripts *v*, *h* are denoting the horizontal and vertical arranged trabeculae; *C* is indicating the origin.

Model I

Trabecula	*Vector* **n** *(x,y,z)*		*Center T (x,y,z)*	
	$\mathbf{n}_v$	$\mathbf{n}_h$	T_v	T_h
left/**t**op	$[\sin(10°), 0, \cos(10°)]$	$[0, \sin(95°), \cos(95°)]$	(-400,0,0)	(0,0,-700)
middle	$[1, 0, 0]$	$[0, 0, 1]$	(0,0,0)	(0,0,0)
right/**b**ottom	$[\sin(15°), 0, \cos(15°)]$	$[0, \sin(95°), \cos(95°)]$	(400,0,0)	(0,0,700)

Table 6.1: Parameters of the oblate ellipsoids utilized in Model I. Units of the centres are given in μm. The susceptibility of the trabecular bone and the bone marrow were set to $\chi_1 = -0.62\cdot 10^{-3}$ and $\chi_2 = -0.9\cdot 10^{-3}$, respectively [22]. A main magnetic field of $\mathbf{H}_0 = 30000$ Gauss, $\alpha = 5°$ and $\beta = 0°$ was applied.

way, that each trabecula was replaced by two ellipsoids, which were displaced along the z-axis by 25 μm forming a crack. The configuration of the two-dimensional vertebra model and the applied parameter setting are given in Fig.6.2 and in Tab.6.3-6.2, respectively.

Dimensions

	Model I		***Model II***	
ellipsoids	$a_{v,h} = 3000\ \mu$m	$b_{v,h} = 100\ \mu$m	$a_v = 3000\ \mu$m	$b_v = 150\ \mu$m
unit cell	volume $= 3.92\ mm^3$		area $= 4.00\ mm^2$	
initial BV/TV	$\varsigma_0 = 0.482$		$\varsigma_0 = 0.35$	

Table 6.2: Dimensions of the ellipsoids, the unit cells and the initial bone volume fractions BV/TV.

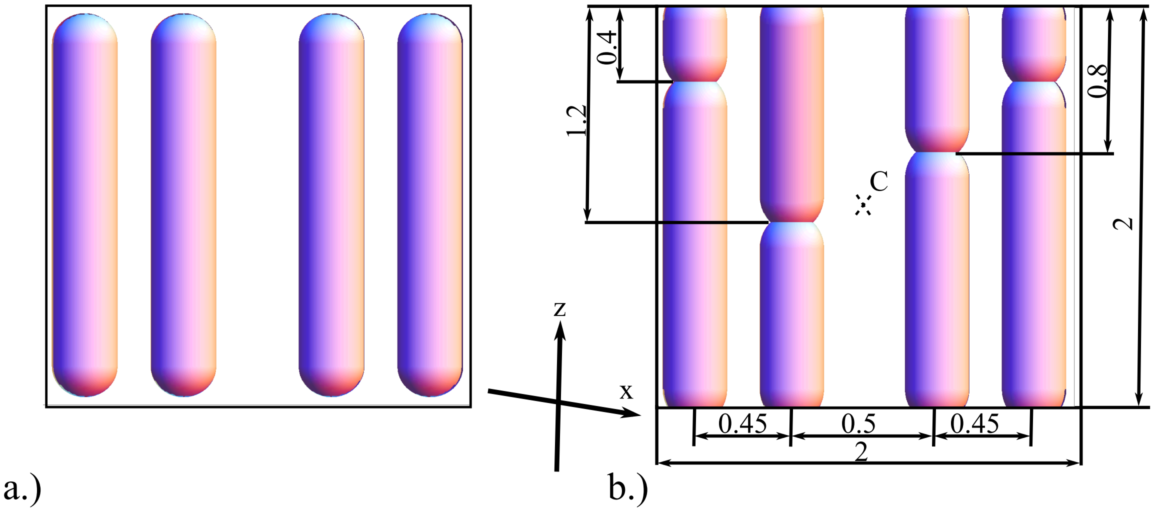

Figure 6.2: a.) Schematic depiction of the four prolate ellipsoids forming the intact two-dimensional rod-like vertebra model; b.) Detailed view of the applied unit cell modelling four trabecular cracks, where the dimensions are given in *mm*. Trabecular microfractures were simulated by replacing each of the intact trabecula with two opposed shifted versions; *C* is indicating the origin.

Model II

Trabecula	*Vector* $\mathbf{n}$ *(x,y,z)*		*Center T (x,y,z)*	
	$\mathbf{n}_{crackA}$	$\mathbf{n}_{crackB}$	T_{crackA}	T_{crackB}
Nr. 1/2	[0,0,1]	[0,0,1]	(-700,0,3500)	(-700,0,-2525)
Nr. 3/4	[0,0,1]	[0,0,1]	(-250,0,1500)	(-250,0,-3525)
Nr. 5/6	[0,0,1]	[0,0,1]	(250,0,3000)	(250,0,-3025)
Nr. 7/8	[0,0,1]	[0,0,1]	(700,0,3500)	(700,0,-2525)

Table 6.3: Parameters of the prolate ellipsoids utilized in Model II. Units of the centres are given in μm. The susceptibility of the trabecular bone and the bone marrow were set to $\chi_1 = -0.62 \cdot 10^{-3}$ and $\chi_2 = -0.9 \cdot 10^{-3}$, respectively [22]. A main magnetic field of $\mathbf{H}_0 = 30000$ Gauss, $\alpha = 30°$ and $\beta = 0°$ was applied.

6.3 Results

6.3.1 Simulating bone loss

In this subsection the results of the analysis studying the impact of loss of bone mass on the field distribution and the resulting relaxation constant T_2' are presented. The histogramms in Fig.6.3 are reflecting the effect of decreasing the bone volume fraction on the field distribution of the reaction fields. Depending on the fraction ς the reaction field H_{r1} approximately varried between -0.6 and -0.05 Gauss. As a consequence of the modelled bone loss the reaction field became more homogeneous, hence the broadness of the histogram narrowed, whereby its maxima was shifted in the direction of a more positive field strength. The simulated signal curves as a function of ς together with the estimated relaxation times are presented in Fig.6.4. The parameters of the least-squares approximation are given in Tab.6.4. The applied Gaussian signal model responded with

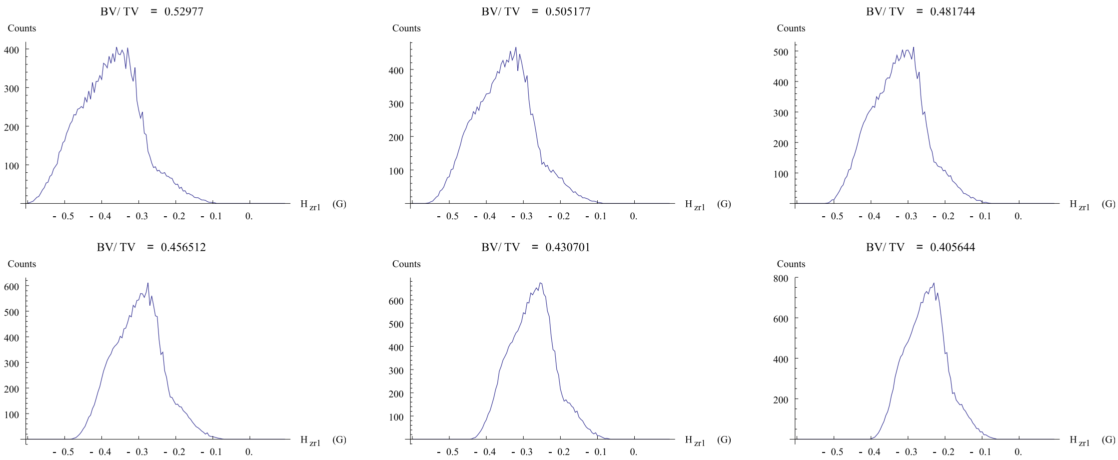

Figure 6.3: Resulting field distributions of the reaction field $H_{r1,z}$ induced by the susceptibility effect between bone and bone marrow. The fields were computed within the entire volume of Model I as a function of ς. A main magnetic field $\mathbf{H}_0 = 30000$ Gauss with $\alpha = 5°$ and β parallel z-axes, and values of $\chi_1 = -0.62 \cdot 10^{-3}$ and $\chi_2 = -0.9 \cdot 10^{-3}$ were applied.

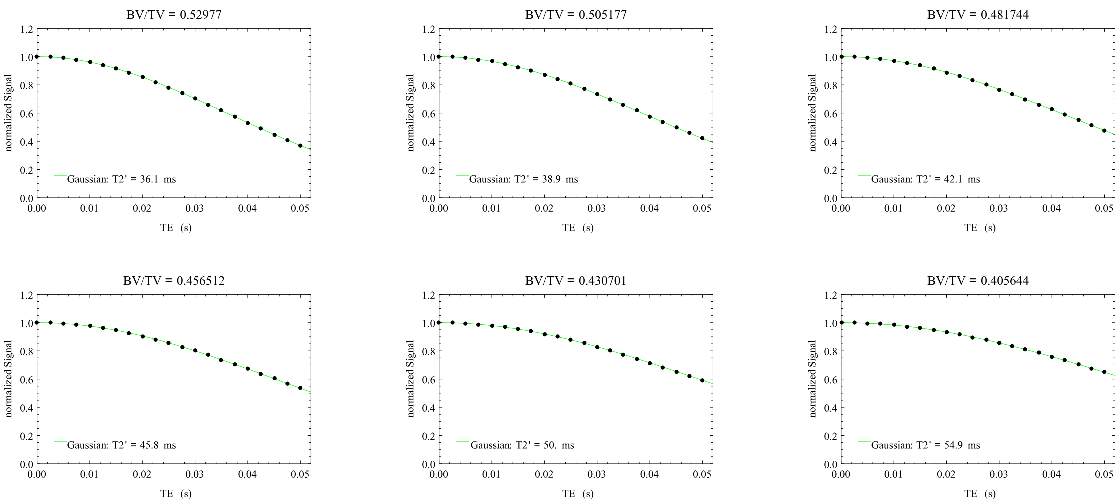

Figure 6.4: Simulated impact of the computed reaction field $H_{r1,z}$ on the MR signal decay. The signals are normalized to the values at the first echo time T_E and presented for various bone volume fractions ς. Markers are indicating the computed signal values at T_E, whereby the green curve was obtained using the estimated parameters of the Gaussian fit-function.

a moderate increase of T_2' with decreasing ς. Further, the Gaussian approach exhibited an almost linear relation between loss of bone mass and the increase of T_2', as can be concluded from Tab.6.4.

In the case of bone disorders such as osteoporosis annual changes of the bone mass between 2–5 % were reported [23, 24]. Applying the presented novel analytical field expressions, such realistic alterations in conjunction with their effects on the MR relaxation parameter T_2' can be studied. In the current simulations minor alterations of $\Delta\varsigma = 0.025$ were successfully modelled, yielding variations of the MR relaxation parameter T_2' in a measurable range of ms. The presented results are qualitatively comparable with previously reported studies, whereby either a different size of the volume of interest or different trabecular elements, rod-like structures, were utilized [19, 25].

6.3.2 Simulating trabecular microcracks

The simulation of the impact of the field disturbances in the vicinity of trabecular cracks on the MR signal time course was carried out through computing the reaction fields along the equatorial plane of the prolate ellipsoids. The interruption was mimiced by forming a gap of 25 μm distance between two opposing trabeculae.

The resulting reaction fields H_{r1} pre- and post bone rarefication are depicted in Fig.6.5. Note, that in the situation of trabecular microfractures significant distortions of the almost homogeneous initial reaction field can be seen. At the transition from the intact to the impaired oseous network significant field variations appear. The field distribution is directly affected by the shape of the microcracks, whereby sharp edges lead to the observed major field distortions. The trabecular rarefication led to an abrupt broadening of the initial narrow resonance spectra. Additionally, around -0.35 Gauss a second local maxima appeared. Prior rarefication, the inital field distribution ranged approximately around ± 0.075 Gauss, afterwards field values from almost -1.5 to 0.4 Gauss were found within the two-dimensional vertebra model.

The effect of the interrupted bone mesh on the MR signal and the resulting estimated relaxation time T_2' is presented in Fig.6.6. The modelled cracks gave rise to a change of the initial T_2' of 196 ms to approximately 15.8 ms.

BV/TV	A_{gau}	B_{gau}	T_2' (ms)	RMSE
0.530	-0.021	1.021	36.10	$0.12 \cdot 10^{-3}$
0.505	-0.029	1.030	38.86	$0.10 \cdot 10^{-3}$
0.482	-0.035	1.035	42.12	$0.07 \cdot 10^{-3}$
0.457	-0.035	1.035	45.78	$0.05 \cdot 10^{-3}$
0.431	-0.038	1.038	49.99	$0.03 \cdot 10^{-3}$
0.406	-0.035	1.035	54.88	$0.02 \cdot 10^{-3}$

Table 6.4: Resulting parameter estimates of the non-linear least-squares approximation of the simulated signal decay to a Gaussian function. The approximations were performed for various ς.

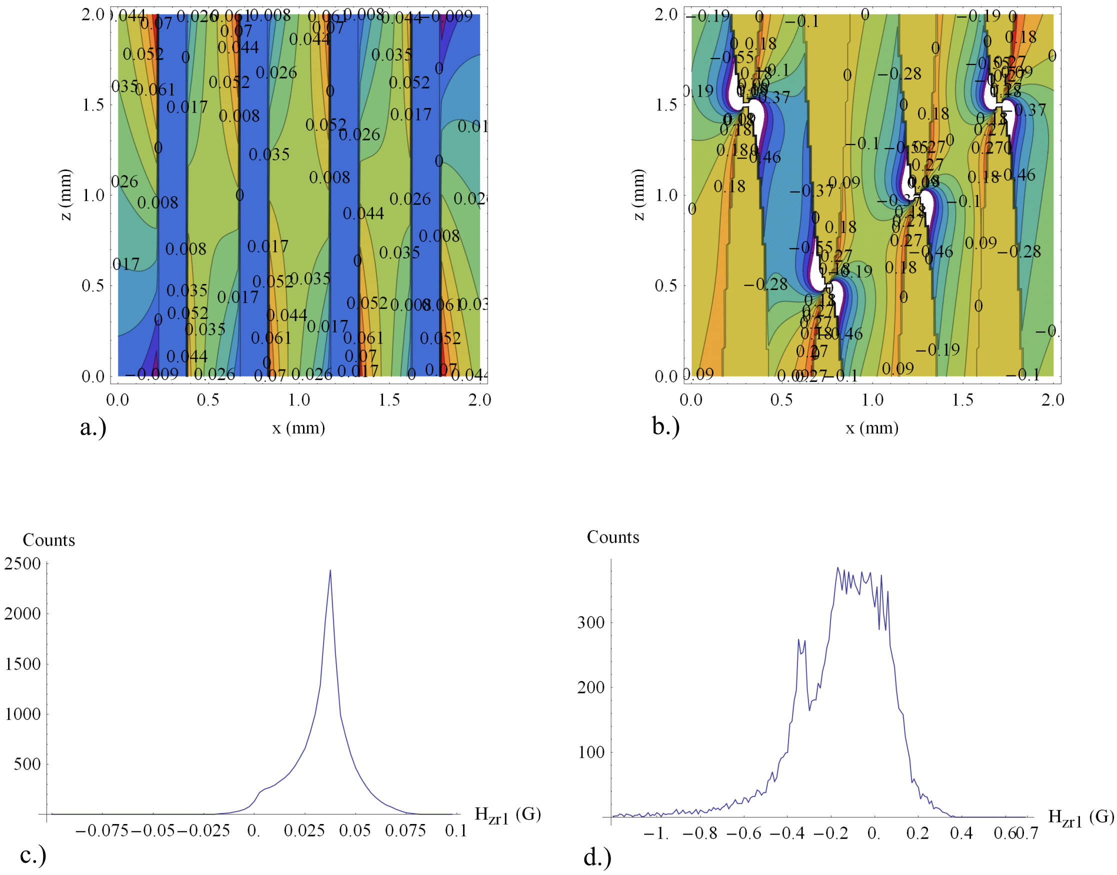

Figure 6.5: Resulting field plot and field distribution depicting the reaction field $H_{r1,z}$ of the applied two-dimensional vertebra model. The situation prior bone rarefication is given in a.) and c.), the impact of trabecular cracks is clearly notable in b.) and d.). A main magnetic field $\mathbf{H}_0 = 30000$ Gauss with $\alpha = 30°$ and β parallel z-axes, and values of $\chi_1 = -0.62 \cdot 10^{-3}$ and $\chi_2 = -0.9 \cdot 10^{-3}$ were applied.

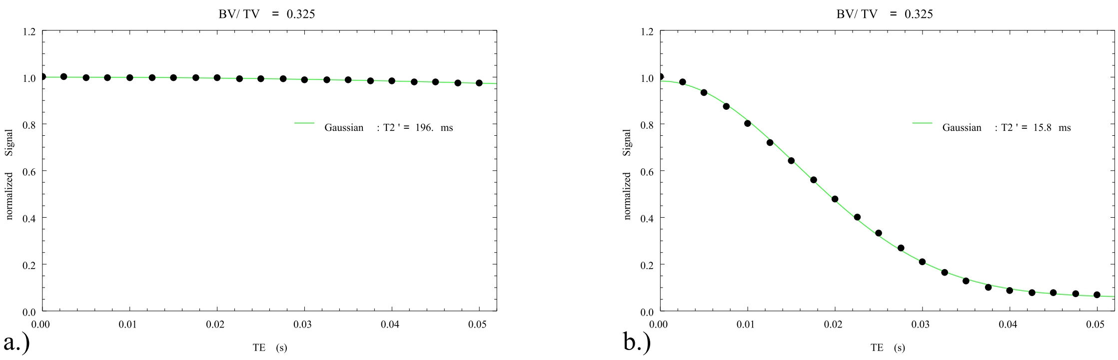

Figure 6.6: Resulting resonance signal decay affected by the reaction field $H_{r1,z}$ within the equatorial x-z plane of the vertebra model. As a consequence of the inhomogeneous reaction field the rapid signal decay is shown in b.). Markers are indicating the computed signal values at T_E, whereby the green curve was obtained using the estimated parameters of the Gaussian fit-function. Further, the signals are normalized to the values at the first echo time T_E.

6.4 Discussion

The analytical solutions of the Laplacian potential problem of spheroids in Cartesian coordinates were successfully applied. Two- and three-dimensional magnetostatic problems in the area of MR-Osteodensitometry were analysed. The performed field simulations are based on previous work of Ford et al. and Selby et al. [18, 19]. Especially the analytical expressions simplified the modelling of arbitrary orientated trabecular bone models in an arbitrary orientated main magnetic field.

To the authors best knowledge for the first time oblate ellipsoids were used to mimic the field effects of plate-like structures more realistically. Such structures made it possible to study the effects of bone mass loss in a basic model of oseous bone. In principle there are no restrictions concerning the amount and orientation of the used oblate spheroids, hence even complex architectures are accessible for modelling.

In a simplified model of a vertebra the susceptibility effects in the vicinity of microcracks were studied. Within vertebrae affected by pathologies such as osteoporosis horizontally arranged structures get typically interrupted at first. The novel expressions make it possible to study the bone rarefication along such pathologies, whereby either cracks of the horizontal, the vertical or arbitrary structures are accessible for modelling. In generall, the use of the analytical field expressions enables the investigation of the induced field distortions in the surrounding of the trabecular microfractures. In an additional study using a more realistic 3D bone model the variations of the reaction fields along the progression of pathological bone remodelling are under investigation. The results of the ongoing study will be published elsewhere.

7 Conclusions

1. Expressions for the potential and field of a prolate spheroid in a homogeneous external field of arbitrary direction have been derived in prolate spheroidal coordinates. These expressions have been transformed to Cartesian coordinates. The resulting expressions have been generalized to an arbitrary direction of the symmetry axis while the external field axis may still have another arbitrary direction.

2. The same has been done for an oblate spheroid with arbitrary symmetry axis and an other arbitrary field axis.

3. Since the magnetic susceptibilites of biological tissues are small ($\approx -10^{-6}$ [26]) it is easy to construct models of trabecular bone structures by arrays of spheroids as described in the two previous items. The total magnetic induction is that of the primary field plus that of all the spheroids in the array to a very good approximation which disregards the small magnetic interaction of the spheroids among themselves.

4. This modelling is particularly easy since all field dependences may be expressed in the same general Cartesian coordinate system.

5. As examples of the method following configurations are treated. Oblate spheroids are used in a 3D model to study the impact of trabecular bone loss on the MR signal decay characteristic. The influence of bone rarefication on the resonance signal is investigated in a simplified 2D model of a vertebra utilizing prolate spheroids.

6. In the present work just one application of the analytical expressions, the modelling of bone disorders in the area of MR-Osteodensitometry, was given. For example in the field of functional MRI the devoloped toolbox eases the analysis of the BOLD (blood oxygenation level-dependent) contrast, where induced reaction fields in the surrounding of vascular networks are of great interest [27]. A fast and precise computation of the magnetic distortion is essential for improving the precision of the temperature determination in techniques using the proton resonance frequency (PRF) shift method [28, 29]. Temperature mapping in the vicinity of the needle electrode is a crucial determinant of MRI guided interventional radiofrequency ablations [30]. Further, in the field of metabolism studies using NMR spectroscopy (MRS) the expressions can be used in order to model specific cells introduced in solutes differing in magnetic susceptibility ! [31].

7. The authors believe that the novel formulation of solutions depending solely on the Cartesian coordinates will facilitate the modelling of countless magnetostatic problems.

Bibliography

[1] PW. Kuchel and BT. Bulliman. Perturbation of homogeneous magnetic fields by isolated single and confocal spheroids. implications for nmr spectroscopy of cells. *NMR*, 2:151–160, 1989. 6, 9, 11, 18, 19

[2] http://itp.tugraz.at/∼schnizer/. 7, 11, 15, 19, 23, 27

[3] Perry Moon and D.E. Spencer. *Field Theory Handbook. Including coordinate systems differential equations and their solutions.* Springer, 1988. 9, 18

[4] M. Kraiger and B. Schnizer. Potential and field of a homogeneous magnetic spheroid of arbitrary direction in a homogeneous magnetic field in cartesian coordinates. *COMPEL, The internat. journal for computation and mathematics in electrical and electronic engineering*, ??:??, 2012/3. 9

[5] M. Kraiger and B. Schnizer. Potential of spheroids in a homogeneous magnetic field in cartesian coordinates. *Proc. 15th International IGTE Symposium, Graz, Austria, 16 to 19 September 2012*, 15:??, 2012. 9

[6] DA. Yablonskiy and EM. Haacke. Theory of nmr signal behavior in magnetically inhomogeneous tissues: The static dephasing regime. *Magnetic Resonance in Medicine*, 32:749–763, 1994. 29

[7] S. Majumdar and HK. Genant. In vivo relationship between marrow t2* and trabecular bone density determined with a chemical shiftselective asymmetric spin-echo sequence. *Journal of Magnetic Resonance Imaging*, 2:209–219, 1992. 29

[8] FW. Wehrli, HK. Song, PK. Saha, and AC. Wright. Quantitative mri of the assessment of bone structure and function. *NMR in Biomedicine*, 19:731–764, 2006. 29

[9] CA. Davis, HK. Genant, and JS. Dunham. The effects of bone on proton nmr relaxation times of surrounding liquids. *Investigative Radiology*, 21:472–7, 1986. 29

[10] S. Grampp, S. Majumdar, M. Jergas, P. Lang, A. Gies, and HK. Genant. Mri of bone marrow in the distal radius: in vivo precision of effective transverse relaxation times. *European Radiology*, 5:43–48, 1995. 29

[11] TM. Link, JC. Lin, D. Newitt, N. Meier, S. Waldt, and S. Majumdar. Computergestützte strukturanalyse des trabekulären knochens in der osteoporosediagnostik. *Der Radiologe*, 38:853–859, 1998. 29

[12] MH. Arokoski, JP. Arokoski, P. Vainio, LH. Niemitukia, H. Kroeger, and JS. Jurvelin. Comparison of dxa and mri methods for interpreting femoral neck bone mineral density. *Journal of Clinical Densitometry*, 5:289–296, 2002. 29

[13] H. Chung, FW. Wehrli, JL. Williams, and SD. Kugelmass. Relationship between nmr transverse relaxation, trabecular bone architecture and strength. *Proceedings of the National Academy of Sciences.*, 90:10250–10254, 1993. 29

[14] TB. Brismar, T. Hindmarsh, and H. Ringertz. Experimental correlation between t2* and ultimate compressive strength in lumbar porcine vertebrae. *Academic Radiology*, 4:426–430, 1997. 29

[15] O. Beuf, DC. Newitt, L. Mosekilde, and S. Majumdar. Trabecular structure assessment in lumbar vertebrae specimens using quantitative magnetic resonance imaging and relationship with mechanical competence. *Journal of Bone and Mineral Research*, 16:1511–1519, 2001. 29

[16] T. Hildebrand, A. Laib, R. Müller, J. Dequeker, and P. Rüegsegger. Direct three-dimensional morphometric analysis of human cancellous bone: Microstructural data from spine, femur, iliac crest, and calcaneus. *Journal of Bone and Mineral Research*, 14:1167–1174, 1999. 29, 31

[17] CJC. Bakker, R. Bhagwandien, MA. Moerland, and M. Fuderer. Susceptibility artifacts in 2d ft spin-echo and gradient-echo imaging: the cylinder model revisted. *Magnetic Resonance Imaging*, 11:539–548, 1992. 30

[18] JC. Ford, FW. Wehrli, and H-W. Chung. Magnetic field distribution in models of trabecular bone. *Magnetic Resonance in Medicine*, 30:373–379, 1993. 30, 37

[19] K. Selby, S. Majumdar, D. Newitt, and HK. Genant. Investigation of mr decay rates in microphantom models of trabecular bone. *Journal of Magnetic Resonance Imaging*, 6:549–559, 1996. 31, 35, 37

[20] A. Fransson, S. Grampp, and H. Imhof. Effects of trabecular bone on marrow relaxation in the tibia. *Magnetic Resonance Imaging*, 17:69–82, 1998. 31

[21] DC. Newitt, S. Majumdar, MD. Jergas, and H. Genant. Decay characteristics of bone marrow in the presence of a trabecular bone network: In vitro and in vivo studies showing a departure from monoexponential behavior. *Magnetic Resonance in Medicine*, 35:921–927, 1996. 31

[22] JA. Hopkins and FW. Wehrli. Magnetic susceptibility measurement of insoluble solids by nmr: Magnetic susceptibility of bone. *Magnetic Resonance in Medicine*, 37:494–500, 1997. 32, 33

[23] S. Harris and B. Dawson-Hughes. Rates of change in bone mineral density of the spine, heel, femoral neck, and radius in healthy postmenopausal women. *Bone and Minearl*, 17:87–95, 1992. 35

[24] JW. Davis, PD. Ross, RD. Wasnich, CJ. MacLean, and JM. Vogel. Long-term precision of bone toss rate measurements among postmenopausat women. *Calcified Tissue International*, 48:311–318, 1991. 35

[25] H-W. Chung, SN. Hwang, HN. Yeung, and FW. Wehrli. Mapping of the magnetic-field distribution in cancellous bone. *Journal of Magnetic Resonance, Series B*, 113:172–176, 1996. 35

[26] JF. Schenck. The role of magnetic susceptibility in magnetic resonance imaging: Mri magnetic compatibility of the first and second kinds. *Medical Physics*, 23:816–850, 1996. 38

[27] S. Ogawa, TM. Lee, AR. Kay, and DW. Tank. Brain magnetic resonance imaging with contrast dependent on blood oxygenation. *Proceedings of the National Academy of Sciences of the United States of America*, 87:9868–9872, 1990. 38

[28] JC. Hindman. Proton resonance shift of water in gas and liquid states. *Journal of Chemical Physics*, 44:4582–4592, 1966. 38

[29] V. Rieke and KB. Pauly. Mr thermometry. *Journal of Mag*, 27:376–390, 2008. 38

[30] A. Boss, H. Graf, B. Müller-Bierl, S. Clasen, D. Schmidt, PL. Pereira, and F. Schick. Magnetic susceptibility effects on the accuracy of mr temperature monitoring by the proton resonance frequency method. *Journal of Magnetic Resonance Imaging*, 22:813–820, 2005. 38

[31] PW. Kuchel. Red cell metabolism: studies using nmr spectroscopy. *Proceedings of Australian Biochemistry Society*, 15:P5–P6, 1983. 38